EPSC2018

LSE4 abstracts

EPSC Abstracts
Vol. 12, EPSC2018-255, 2018
European Planetary Science Congress 2018

A novel data processing technique for detection of deep subsurface echoes of lunar maria by Kaguya Lunar Radar Sounder

Takao Kobayashi, Seung Ryol Lee, and Kyo-Yeong Song
Korea Institute of Geoscience and Mineral Resources, Korea (tak@kigam.re.kr)

Abstract

A technique to enhance weak radar signals of deep subsurface echoes was developed for the purpose of identifying a deep subsurface boundary interface in the lunar subsurface. The technique comprises of two sub-techniques: one is mean subtraction technique and another is data stacking technique. The mean subtraction technique subtracts the mean value from the observation data so as to enhance small variation of the target signal whereas the data stacking technique stacks data acquired from a few orbits to enhance echo image pattern. The technique was applied to radargram image data of Kaguya Lunar Radar Sounder. The preliminary application successfully detected a deep boundary interface at an apparent depth of 2 km in Mare Crisium, which had been previously unknown.

1. Introduction

Volcanism is the important geologic event in the early history of the Moon. Volume of lava that filled basins to make today's maria is the key parameter to quantitatively evaluate the lunar volcanism. The lava volume is evaluated based on the information of lava layer thickness.

Currently the only source of lava layer thickness information is Kaguya Lunar Radar Sounder (LRS) data [1]. LRS was an HF radar whose observation frequency was 5 MHz. LRS was an on-board science mission of Kaguya, a lunar exploration program of Japan, which was launched in 2007 and finished its operation in 2009. The primary objective of LRS was subsurface geologic structure of the Moon. LRS carried out global survey of the Moon, and its footprint covered almost entire surface of the Moon during the mission period. LRS detected subsurface "reflectors", or subsurface boundary interfaces, in maria, but, against initial anticipation, the detection points were located only in limited areas in maria [1, 2]. Furthermore, the depths of those detected subsurface reflectors were much shallower than those which had been expected [1].

We developed a technique to process radargram image data of LRS for detecting weak echoes from a deep subsurface reflector. This paper describes the technique, and presents an application result of Mare Crisium observation.

2. Data processing

Our data processing technique comprises of two techniques; one is 'mean subtraction' and another is 'image data stacking.'

2.1 Mean subtraction

A radargram is regarded as a 2-dimensional image data set, $I(x,r)$, which is a function of two variables, observation position, x, and observation range, r. $I(x,r)$ may be expressed as

$$I(x,r)=I_0(r)+\Delta I(x,r) \qquad (1)$$

where $I_0(r)$ is the mean range-echo profile and $\Delta(x,r)$ is small residual term representing either surface clutter or subsurface echo. $I_0(r)$ a function of only the observation range and is defined as

$$I_0(r) = \frac{1}{N}\sum^{N} I(x_n, r) \qquad (2)$$

A subsurface reflector is recognized as a horizontal pattern image in a radargram which is made of appearance of a number of $\Delta(x,r)$ at a depth. If

$$I_0(r) \gg \Delta I(x,r), \qquad (3)$$

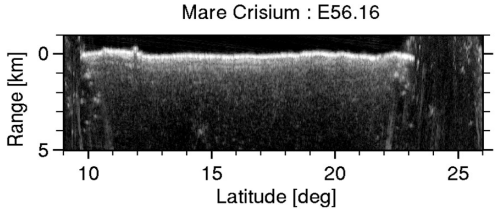

Figure 1: A radargram of LRS observation of Mare Crisium.

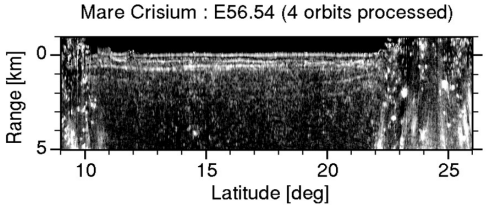

Figure 2: Produced radargram after the proposed process. Observation data of closely located four orbits including that of Fig. 1were processed.

then, $I_0(r)$ would dominate $\Delta I(x,r)$ so that $\Delta I(x,r)$ would be omitted in $I(x,r)$. In such a case, however, if $I_0(r)$ is removed from $I(x,r)$, then $\Delta I(x,r)$ would be easily recognized. We first calculate $I_0(r)$ after Eq. (2), then subtract it from $I(x,r)$ to obtain $\Delta I(x,r)$.

2.2 Image data stacking

Though weak echoes can be recognized now, clutters are also more conspicuous. However the subsurface boundary echoes appear in rather coherent fashion at limited depths around boundary interfaces while clutters appear in a random manner at all depths. We make use of these natures to distinguish weak subsurface echoes by stacking more than one set of $\Delta(x,r)$.

3. Result

Figure 1 shows a radargram presentation of LRS data which were acquired over Mare Crisium along a longitudinal line at E56.16 degrees. The data are released SAR-processed data [3] with a synthetic aperture 5 km. Shallow subsurface reflector echoes are recognized at apparent depths (ranges) shallower than 1 km, however none but clutters can be recognized at deeper depth than 1 km.

Figure 2 shows a radargram which was produced by the proposed technique. The data were acquired from closely located four orbits along longitudinal lines of E56.16, E56.52, E56.72, and E56.74. The process obviously improved visibility of subsurface reflector echoes: the echoes from depths shallower than 1 km appear more prominent while those from deeper reflectors are now recognized. The depth of the deepest reflector echo is measured as 2 km in the radargram.

4. Conclusion

This paper described newly proposed technique which is to be applied to the LRS data for the purpose of improving detectability of weak subsurface echoes. An application example showed previously unknown deep weak subsurface echoes at an apparent depth of 2km in Mare Crisium.

Acknowledgements

This work is supported by the basic research 18-3111-1 of Korea Institute of Geoscience and Mineral Resources.

References

[1] Ono, T. et al.: Lunar Radar Sounder observation of subsurface layers under the nearside maria of the Moon, Science, Vol. 323, pp. 909 – 912, 2009, DOI: 10.1126/science.1165988.

[2] Pommerol, A. et al.: Detectability of subsurface interfaces in lunar maria by the LRS/SELENE sounding radar: Influence of mineralogical composition, G.R.L, 2010, Vol. 37, L03201.

[3] SELENE data archive, JAXA, http;//darts.isas.jaxa.jp/planet/pdap/selene/index.html.en.

EPSC Abstracts
Vol. 12, EPSC2018-388, 2018
European Planetary Science Congress 2018

Diviner Lunar Radiometer Highlights from the LRO Cornerstone Mission

Benjamin T. Greenhagen (1), David A. Paige (2), and the Diviner Lunar Radiometer Science Team
(1) Johns Hopkins Applied Physics Laboratory, Luarel, MD, USA, (2) University of California Los Angeles, Los Angeles, CA, USA (benjmain.greenhagen@jhuapl.edu)

Abstract

After over nine years in operation NASA's Lunar Reconnaissance Orbiter (LRO) Diviner Lunar Radiometer (Diviner) continues to reveal the extreme nature of the Moon's thermal environments, thermophysical properties, and surface composition. Diviner is the first multispectral thermal infrared instrument to globally map an airless body with relatively high spatial and temporal resolution. Thus Diviner observations form a cornerstone of thermal infrared studies of the Moon and airless bodies with important considerations for future datasets from the Moon, Mercury, small bodies, and icy satellites.

1. Diviner Lunar Radiometer

To date, Diviner has acquired observations over 18 complete diurnal cycles and 8 seasonal cycles. Diviner daytime and nighttime observations have essentially global coverage, and more than 90% of the surface has been measured with at least 8 different local times. Diviner's extended operations have also enabled observations of the lunar surface with a wide range of viewing geometries. The spatial resolution during the mapping orbit was ~200 m and now ranges from 150 m to 1300 m in the current elliptical orbit. Calibrated Diviner data and maps of visible brightness, temperature, rock abundance, nighttime soil temperature, and silicate mineralogy are available through NASA's Planetary Data System Geosciences Node.

Diviner was designed to accurately measure temperatures across a broad range from midday equatorial regions such as the Apollo sites (around 400K), typical nighttime temperatures of less than 100K, and extreme permanent shadowed regions colder than 50K. The coldest multiply-shadowed polar craters may have temperatures low enough constrain lunar heat flow [1]. Nighttime temperatures are driven by the thermophysical properties, including rock abundance and soil thermal inertia, which are used to investigate impact crater formation and evolution processes [2]. Multichannel infrared spectroscopy can constrain silicate mineralogy, including compositional heterogeneity in the lunar crust [3]. In addition to lunar properties, during the current LRO Cornerstone Mission (CM), we use new observation campaigns to characterize thermal emission behaviour fundamental to airless bodies with fine-particulate surfaces, including epiregolith thermal gradients and thermal-scale surface roughness.

2. Cornerstone Mission

With a vast dataset of nadir-pointing diurnal data on hand, we now look to use Diviner's spacecraft-independent gimballing capabilities to make special regional and global observations. Approximately half of Diviner data from the CM are one of four types of special observations: Lunar eclipse, twilight campaigns, targeted off-nadir EPFs, and global off-nadir campaigns.

2.1 Lunar Eclipses

The sharp thermal pulse associated with lunar eclipse provides the best opportunity to study the thermophysical structure of the upper few cms on the regolith. However, eclipses are infrequent and observations are limited to areas around the LRO ground track. Additionally, Diviner is no longer allowed to make measurements during total lunar eclipses due to spacecraft power restrictions. Therefore during the CM, we focus on partial lunar eclipses where these key observation can be for the portion of the Moon that is in total Earth shadow. We observed one partial eclipse on 7 August 2017 and will observe a second one in July 2019.

2.2 Twilight Campaigns

While there are limited opportunities to view lunar eclipses, all areas on the Moon experience rapid temperature drops immediately after local sunset. However, this analysis requires very high temporal density coverage across lunar "twilight." During the CM, we target ROIs for repeated observation on adjacent orbit tracks (~4 lunar minutes apart) during the 17:45 to 18:45 time period. The LRO orbit affords us opportunities to makes these measurements nearly globally and in many areas there are multiple opportunities.

2.3 Targeted Off-Nadir EPFs

The lunar surface is both very rough and highly insulating on scales of mm to cm, which produces range of temperatures (i.e. anisothermality) within any scene [4]. To fully characterize this behaviour requires multispectral thermal infrared observations with systematically varying viewing and illumination geometries. The improved understanding of the lunar regolith emission phase function (EPF) will feed directly into models of heat transfer on airless bodies and volatile transport and sequestration. During the CM, we will measure EPFs for ten representative targets.

2.4 Global Off-Nadir Campaigns

During the CM we will produce global maps with approximately 50 degree emission angles, both low and high phase at eight different local times (four day and four night). These data compliment an existing 70 degree emission angle, low phase campaign and enable an extension of the targeted EPF science to global scales.

3. Summary

This presentation will focus on recent Diviner results addressing a diverse range of scientific questions and will highlight exciting new observations from LRO's Cornerstone Mission.

References

[1] Paige & Siegler (2016) LPSXLVII, Abstract #2753.

[2] Ghent et al. (2014) Geology, 42, 1059-1062.

[3] Greenhagen et al. (2010) Science, 329, 1507-1509.

[4] Bandfield et al. (2014) Icarus, 248, 357-372.

EPSC Abstracts
Vol. 12, EPSC2018-473, 2018
European Planetary Science Congress 2018

Moon South Pole Mapping by LEND Instrument

Anton Sanin(1), Igor Mitrofanov(1), Maxim Litvak(1), Boris Bakhtin(1), William Boynton(2), Gordon Chin(3), Karl Harshman(2), Dmitry Golovin(1), Alexander Kozyrev(1), Timothy Livengood(3), Alexey Malakhov(1), Timothy McClanahan(3), Maxim Mokrousov(1), Richard Starr(3), Roald Sagdeev(4), Vladislav Tret'yakov(1), Andrey Vostrukhin(1) (1) Space Research Institute, Moscow, Russian Federation, (2) Lunar and Planetary Laboratory, University of Arizona, Tucson, AZ 85719, USA, (3) NASA Goddard Space Flight Center, Greenbelt, MD 20771, USA, (4) University of Maryland, College Park, MD 20742, USA

Abstract

The Lunar Exploration Neutron Detector (LEND) is operating on orbit around the Moon on-board the Lunar Reconnaissance Orbiter (LRO) spacecraft more than eight years since LRO launch at June 18, 2009. The primary scientific goals for the LEND experiment is to investigate presence and determine average amount of hydrogen in upper (~1 m depth) subsurface layer of the Lunar regolith with high spatial resolution and to test the hypothesis what the permanently shadowed regions (PSRs) at circumpolar regions are the main reservoirs of a large deposition of water ice on the Moon [1,2].

It was found [3,4] from the LEND observations what not all large PSRs contain a detectable amount of hydrogen but there are neutron suppression regions (NSRs) with statistically significant suppression of neutron flux. The NSRs partially overlap or include PSRs in craters Cabeus, Shoemaker, Haworth (on South) and Rozhdestvensky U (on North) but significant part of their area spread out at sunlit terrains [5,6]. This means what hydrogen may exist under a thin dry regolith layer. The majority of PSRs do not contain any significant additional concentrations of hydrogen in comparison with the sunlit areas around them. In addition, the specially developed method allows to estimate the water equivalent hydrogen (WEH) in top ~1 meter regolith using LEND data [7]. These publications uses the LEND dataset from September 16, 2009 until April 1, 2015.

Now we have a three additional years of data accumulation in the LEND experiment. Therefore, in this talk, we would present the updated maps of epithermal neutron counting rate and WEH for the South Polar region. Some interesting local areas (Cabeus and Shoemaker craters) will be discussed in more details.

References

[1] Mitrofanov I. G. et al.: Experiment LEND of the NASA Lunar Reconnaissance Orbiter for High-Resolution Mapping of Neutron Emission of the Moon, Astrobiology, Volume 8, Issue 4, pp. 793-804, 2008, DOI:10.1089/ast.2007.0158

[2] Mitrofanov I. G. et al.: Lunar Exploration Neutron Detector for the NASA Lunar Reconnaissance Orbiter, Space Science Reviews, Volume 150, Issue 1-4, pp. 183-207, 2010, DOI:10.1007/s11214-009-9608-4

[3] Litvak M.L. et al.: Global maps of lunar neutron fluxes from the LEND instrument, Journal of Geophysical Research, Volume 117, CiteID E00H22, 2012, DOI:10.1029/2011JE003949.

[4] Mitrofanov I. G. et al.: Testing polar spots of water-rich permafrost on the Moon: LEND observations onboard LRO, Journal of Geophysical Research, Volume 117, CiteID E00H27, 2012, DOI:10.1029/2011JE003956.

[5] Boynton, W. V. et al.: High spatial resolution studies of epithermal neutron emission from the lunar poles: Constraints on hydrogen mobility, Journal of Geophysical Research, Volume 117, CiteID E00H33, 2012, DOI:10.1029/2011JE003979.

[6] Sanin A.B. et al.: Testing lunar permanently shadowed regions for water ice: LEND results from LRO, Journal of Geophysical Research, Volume 117, CiteID E00H26, 2012, DOI:10.1029/2011JE003971.

[7] Sanin A.B. et al.: Hydrogen distribution in the lunar polar regions, Icarus, Volume 283, Pages 20–30, 2017, DOI:10.1016/j.icarus.2016.06.002

EPSC Abstracts
Vol. 12, EPSC2018-482, 2018
European Planetary Science Congress 2018

Investigation Recent Impacts with Temporal Image Pairs and Photometric Sequences

Emerson Speyerer (1), Robert Wagner (1), Reinhold Povilaitis (1), Aaron Boyd (1), Mark Robinson (1) and Brett Denevi (2) (1) School of Earth and Space Exploration, Arizona State University, Tempe, AZ, (2) Planetary Exploration Group, Johns Hopkins University Applied Physics Laboratory, Laurel, MD (emerson.speyerer@asu.edu)

Abstract

Temporal observations and follow-up photometric sequences by the Lunar Reconnaissance Orbiter Camera (LROC) enable the detection and analysis of newly formed impact craters. From the temporal pairs we can locate new craters and identify up to four distinct reflectance zones surrounding the impact site. Photometric sequences acquired after the impact reveal a higher backscatter signature associated with several of the reflectance zones.

1. Introduction

The Lunar Reconnaissance Orbiter (LRO) extended mission is enabling the discovery and investigation of recent surface changes. An initial investigation led to the discovery of over 200 newly formed impact craters and 47,000 secondary surface disturbances and unresolved primary impact craters [1]. Additional temporal observations have led to the discovery of over 200 more craters and 76,000 other changes. Photometric sequences acquired during the Cornerstone Mission (Sept 2016-present) are enabling us to further study these new surface features and provide insight into the cratering process.

2. Temporal Imaging

We can identify new surface features by comparing images that cover the same surface area with nearly identical lighting conditions. We compared WAC global mosaics captured between April 2012 and January 2016 to identify several primary impact craters ranging in size between 30 and 70 m in diameter. While these craters are smaller than a single WAC pixel, the disturbance around each crater extends several km in many cases allowing us to locate them and target NAC images to confirm the formation and gather crater size statistics.

Direct comparisons of NAC images to other NAC images with similar lighting conditions (incidence angle difference < 3°) enables us to identify hundreds of additional craters down to the resolution limit of the NAC (several meters). During the initial study [1], NAC temporal image pairs had an average time difference between observations of 1.3 years. Due to the progression of the orbit and the illumination environment, LROC started collecting temporal pairs in November of 2017 with a baseline of 7.3 years. The longer baseline increases the odds of a surface change occurring over the imaged terrain and improves our coverage statistics. Additional long baseline temporal observations between 7 and 10 years will continue to be acquired during the third year of the Cornerstone Mission and the next Extended Mission.

Temporal ratio images created by dividing the after image by the before image are used to identify changes to the surface reflectance. Because the lighting and viewing geometries are similar and the images are spatially registered, the values in the temporal ratio image are close to one except in cases where a reflectance change has occurred on the surface, such as a ray forming from a new impact.

3. Photometric Sequences

Once a prominent new surface feature is discovered, we can target follow-up observations. For a select number of the larger, newly formed impact craters (> 30 m), we are targeting photometric sequences and geometric stereo pairs. Each month LROC can observe the newly formed crater under a different illumination environment. By comparing reflectance measurements from images acquired over many months, we can evaluate the phase curve of small regions of the surface around the site. To reduce the effects of varying incidence angle, we can also target photometric sequences where images of the site are acquired on consecutive orbits (phase and emission

angles vary, incidence angle remains nearly constant). In addition, sometimes as part of the same sequence, a NAC geometric stereo pair is collected. These stereo observations allow us to create digital terrain models (DTMs) to examine the topography of the site [2]. The DTMs can also be used to calculate the incidence and emission angles relative to local topography, thus allowing the effects of topography to be remove when applying a photometric correction. With the sum of these observations, we can account for the dependence of reflectance on the observational geometry (incidence, emission, and phase) and investigate how the physical properties of the regolith (such as grain size, roughness, and porosity) affect the way light is reflected [e.g., 3].

4. Newly Formed Impact Craters

To date, we have discovered over 400 newly formed craters using LROC temporal imaging. Temporal image ratios of the before and after images reveal up to 4 reflectance zones around the new impact craters [1, 4]:

- Proximal high reflectance zone (PHRZ)
- Proximal low reflectance zone (PLRZ)
- Distal high reflectance zone (DHRZ)
- Distal low reflectance zone (DLRZ)

These changes in the surface reflectance are caused by exposure of immature regolith as well as changes in the regolith properties. In addition, phase ratio images, which are collected as part of a photometric sequence, are created by taking the ratio of a low phase image over the high phase image with similar incidence angle (i.e., $p(g_1)/p(g_2)$; where $g_1<g_2$ and $i_1 \approx i_2$) [5]. These phase ratio images allow one to assess the slope of the phase function and compare it to the surrounding, undisturbed regolith.

Figure 1 shows an example of a temporal ratio image and phase ratio image of a new 26 m crater whose impact flash was observed on Earth on 11 September 2013 [6]. In the temporal ratio, a PHRZ and PLRZ is visible immediately adjacent to the crater. Both proximal regions in the phase ratio image appear brighter than the background, indicating a steeper phase function between 31° and 64°. In addition, there is no clear differentiation in the phase ratio image between the two distinct proximal zones visible in the temporal ratio image. The PHRZ and PLRZ are interpreted to be the immature and mature material (respectively) of the continuous ejecta blanket [1]. The steeper phase function indicates increased backscattering that could be caused by increased surface roughness. Additional bright rays in the phase ratio image extend several km from the impact site indicating increased backscatter and roughening of the regolith or an increase in the local porosity. Some of these rays correspond to the DLRZ in the temporal image pair that Speyerer et al. [1] interpret to be caused by sparse ballistic sedimentation or impact induced jetting from the primary impact event.

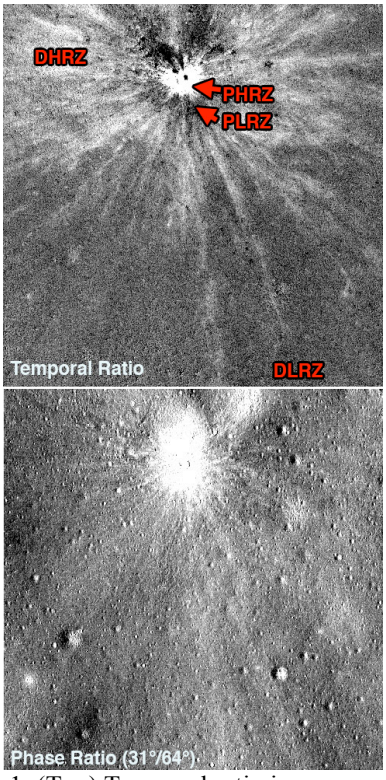

Figure 1: (Top) Temporal ratio image created by taking the ratio of M1149637354LR (2014-075) and M1119014742LR (2013-086) of a new 26 m crater. (Bottom) Phase ratio image created by taking the ratio of M1151986536LR (i=46°, e=17°, g=31°) with M1152000776LR (i=44°, e=21°, g=64°). Each image is 1300 m across.

5. References

[1] Speyerer et al. (2016) *Nature*, 258, 215-218. [2] Henriksen et al. (2017) *Icarus*, 283, 122-137. [3] Hapke (2012) *Theory of Reflectance and Emittance Spectroscopy*. [4] Robinson et al. (2015) *Icarus*, 252, 229–235. [5] Kaydash (2011) *Icarus*, 211, 89-96. [6] Madiedo et al. (2014) Mon. Not. R. Astron. Soc. 439, 2364–2369.

EPSC Abstracts
Vol. 12, EPSC2018-492, 2018
European Planetary Science Congress 2018

Far-Ultraviolet Investigation of New Impact Craters and Cold Spots on the Moon Using the LRO LAMP Data

Y. Liu (1), K. D. Retherford (2,3), T. K. Greathouse (2), K. E. Mandt (4), J. T. S. Cahill (4), A. R. Hendrix (5), U. Raut (5), C. Grava (2), B. Byron (3,2), L. O. Magaña (3,2), A. F. Egan (6); (1) Lunar and Planetary Institute, Houston, TX, USA (liu@lpi.usra.edu), (2) Southwest Research Institute, San Antonio, TX, USA, (3) University of Texas at San Antonio, San Antonio, TX, USA, (4) Johns Hopkins University Applied Physics Laboratory, Laurel, MD, USA, (5) Planetary Sciences Institute, Tucson, AZ, USA, (6) Southwest Research Institute, Boulder, CO, USA

Abstract

We present the far-ultraviolet (FUV) observations of new impact craters and cold spots on the Moon using LRO LAMP data. Our results show distinct spectral response to these features in FUV wavelengths.

1. Introduction

The Lunar Reconnaissance Orbiter (LRO) Lyman Alpha Mapping Project (LAMP) provides global coverage of both nightside and dayside of the Moon in the far ultraviolet (FUV) wavelengths between 57 and 196 nm [1]. The innovative nightside observations use roughly uniform diffuse illumination sources from interplanetary medium Lyman-α sky glow and UV-bright stars. The dayside observations use the more traditional photometry technique with the Sun as the illumination source which is very complementary.

Global albedo maps are produced at Lyman-α, on-band and off-band, which are used to constrain the abundance of water frost based on the strength of the on and off the water frost absorption edge at ~165 nm [1]. The nightside FUV albedo measurements over a few PSRs in south pole indicate 1-2% water frost abundances [2]. The dayside data reveals a distinct diurnal variation in hydration level across the surface of the Moon [3]. The spectral images cubes with 2 nm resolution are created to characterize lunar swirls for several regions of interests by the reddened FUV spectra of immature materials [4].

In this work, we introduce photometric corrections for LAMP dayside observations. We investigate the spectral properties of new impact craters detected by LROC instrument and cold spots identified by DIVINER instrument, using LAMP FUV data.

2. Photometric Correction

LAMP dayside observations use sunlight as the illumination source where bidirectional reflectance is measured. The bidirectional reflectance is dependent both upon the observation geometry and the soil properties. To compare the same area covered from multiple observations with different viewing geometries, photometric corrections are needed to normalize the reflectance as if it is measured in the same observation geometry. In this work, we use a simplified Hapke's bidirectional reflectance distribution function (BRDF) to simulate LAMP's reflectance [5]. By modeling the lunar phase curve (i.e., reflectance as a function of phase angles) at FUV wavelengths, we retrieve the wavelength-dependent Hapke parameters by using the Levenberg-Marquardt regression analysis algorithm. The retrieved Hapke parameters are then used for photometric corrections of LAMP data using the Hapke BRDF model. The photometrically corrected data will be used to investigate the new impact craters and cold spots on the Moon.

3. New Impact Craters

Numerous new craters have been detected by LROC NAC paired observations [7]. For example, more than 200 new impact craters have formed in past 9 year, which indicates that new craters are forming on the surface of the moon more frequently than model had predicted [7]. These new impact events excavate new materials from the subsurface of the Moon, and also the impact induced jetting or scouring has potentially modified the lunar surface in a great distance. Our initial analysis over a 70 m diameter new crater, formed in Mare Humorum in October 2012, shows distinct overall albedo changes at FUV wavelengths before and after impact. Figure 1 shows the albedo at 165 nm before and after impact as a

function of distance to the impact center. After impact, the albedo increases significantly especially within 100 km radius of the impact. The albedo generally decreases with increase of the distance, but the albedo differences are even visible at 150 km away from the impact, indicating the great influence of the impact during the formation of this 70 m crater.

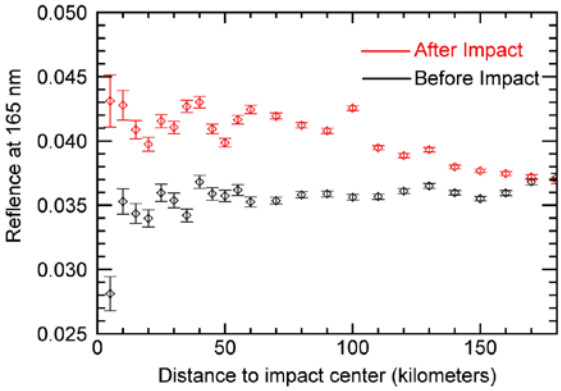

Figure 1: Reflectance at 165 nm before and after impact as a function distance to the impact site.

4. Cold Spots

A class of anomalous cold surfaces (termed "cold spots") has been identified by Diviner radiometer [8]. These "cold spots" are mostly associated with fresh craters with unique ejecta morphology. Cold spots extent ~30-60 crater radii, which have rayed profiles that mimic the visible proximal ejecta deposits. However these cold spot features cannot be explained by the emplacement of ejecta alone. Specifically, there is no spectral/albedo evidence of deposition and/or scouring from visible and near infrared data [8]. Our analysis over cold spots using LAMP FUV data, however, shows distinct spectral signatures. We initially analyzed three cold spots and our results consistently show that the cold spot surfaces tend to be more mature than the center fresh crater but are less mature than surrounding terrains (Figure 2). The results indicate that the FUV data are likely more sensitive to the regolith modification over the cold spot surfaces than longer wavelengths, or the disruption of the regolith by exacting or depositing new materials or by impact induced jetting or scouring over cold spot surfaces are more profound than previous thought.

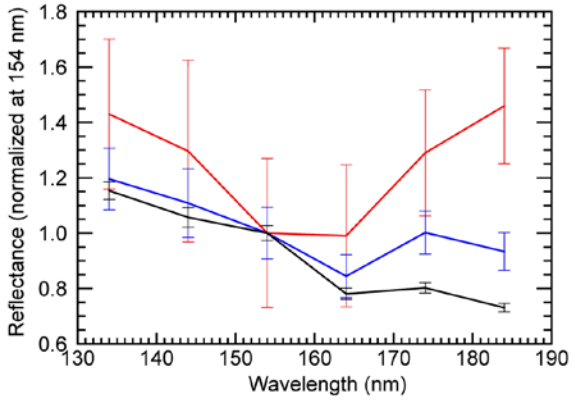

Figure 2: FUV reflectance spectra over the center fresh crater (in red), cold spot surfaces (in blue), and surrounding terrains (in black), respectively, for a representative cold spot.

References

[1] Gladstone, G. R. et al.: LAMP: The Lyman Alpha Mapping Project on NASA's Lunar Reconnaissance Orbiter Mission, Space Sci. Rev., 150, 161-181, 2010.

[2] Gladstone, G. R., et al.: Far-ultraviolet reflectance properties of the Moon's permanently shadowed regions, J. Geophys. Res., 117, E00H04, 2012.

[3] Hendrix, A. R., et al.: The lunar far-UV albedo: Indicator of hydration and weathering, J. Geophys. Res., 117, E12001, 2012.

[4] Hendrix, A. R., et al.: Lunar swirls: Far UV characteristics, Icarus, 273, 68–74, 2016.

[5] Hapke, B.: Theory of Reflectance and Emittance Spectroscopy, Cambridge Univ. Press, New York, 2012.

[6] Cahill J. T. S, et al.: Scrutinizing the presence of LAMP identified plausible lunar swirls relative to magnetic sources, LPSC, Abstract #2964, 2018

[7] Speyerer, E. J. et al.: Quantifying crater production and regolith overturn on the Moon with temporal imaging, Nature, 538, 215-218, 2016

[8] Bandfield, J. L. et al.:,Lunar cold spots: Granular flow features and extensive insulating materials surrounding young craters, Icarus, 231, 221-231, 2014.

EPSC Abstracts
Vol. 12, EPSC2018-575, 2018
European Planetary Science Congress 2018

Reviewing the contribution of GRAIL to lunar science and planetary missions

Maria T. Zuber and David E. Smith
Department of Earth, Atmospheric and Planetary Sciences, Massachusetts Institute of Technology, Cambridge, MA 02139-4307, USA. (zuber@mit.edu, smithde@mit.edu)

Abstract

The GRAIL Discovery mission to the Moon in 2011 provided an unprecedentedly accurate gravity field model for the Moon. The goal of the mission was to provide insight into the structure of the Moon from its interior to the surface but it also made significant contributions to lunar spacecraft operations for all future lunar missions to the Moon. We discuss the science and the broader contributions from this mission that completed its objectives in December 2012 when the spacecraft impacted the lunar surface.

1. Introduction

GRAIL was a mission designed to measure the gravity field of the Moon with both high accuracy and high resolution. The measurement goal was to obtain the gravity at resolutions that would enable interpretation of the crust at fractions of its thickness, estimated at the time of launch to be about 45 km. To obtain a surface resolution of less than 10 km required the spacecraft to orbit the Moon at less than 20 km, an altitude that was considered dangerous at that time without an accurate gravity field model. Thus, the operational plan for GRAIL was to initially fly at about 50 km altitude, obtain a good gravity model, lower the orbit to near 20 km, further improve the gravity model and if successful, lower the orbit to nearer 10 km altitude. With the range of lunar topography reaching about 18 km the spacecraft could be expected to be only a few km above the surface during parts of its orbit [1-3].

2. Science

The science accomplishments of GRAIL [4-7] include (1) the discovery of very high correlation (0.98) of gravity and topography at crustal wavelengths between 100 to 20 km, (2) the crustal thickness to be only 35 km, (3) the mean crustal density of ~2550 kg m^{-3}, (4) the tidal Love number, k2 measured to better than 1% along with its monthly periodicity, (5) the k3 tide was detected, and (6) the Q of the Moon determined to be 41±4 at the monthly frequency.

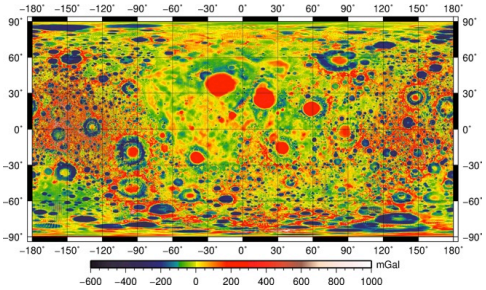

Figure 1: Free-air gravity of the Moon from GRAIL. Full uniform resolution spherical harmonic models were obtained out to degree & order 1200 with special fields with higher resolutions over certain areas to degree and order 1800.

3. Mission Operations

The significant improvement in our knowledge of the gravity field of the Moon by GRAIL enabled the re-analysis of the orbits of past and present lunar orbiting spacecraft, most notably the Lunar Reconnaissance Orbiter (LRO). LRO had been launched 2 years earlier than GRAIL to identify and locate future landing sites. The improvement of the accuracy of the orbit of LRO and the spacecraft's position by GRAIL increased the value of nearly all the instrument datasets but particularly the geodetic instruments, the laser altimeter and the camera.

The laser altimeter data provided very high resolution shape and topography of the Moon and the camera was able to image sites of strategic value and provide accurate positional knowledge of features at the few meter level.

Operationally, the improvement in the gravity field required less frequent orbital predictions for LRO and less tracking of the LRO spacecraft by the microwave network of Doppler tracking stations while exceeding the requirements of the mission.

The GRAIL gravity model was also used to re-determine the orbits of previous lunar missions, including Prospector, and subsequently the LADEE mission that studied dust concentrations down to about 20 km altitude in the lunar equatorial region.

4. Future Mission Applications

GRAIL was a dual spacecraft system in which the 2 spacecraft tracked each other to provide the gravity field data. Both spacecraft were launched together, separated shortly after, and each travelled independently to the Moon. This launch and mission architecture has now been considered for other planet gravity missions, including Mars, Venus, Europa, and even the Sun. However, at none of these potential destinations will it likely be possible to get the equivalent surface resolution that was obtained at the Moon due to the inability to fly close within a few 10's of km of the surface due, principally, to the present of an atmosphere that limits lifetime. Thus the GRAIL gravity model is likely to remain the most precise high resolution field of any planetary body for some time.

Acknowledgements

The GRAIL Science team gratefully acknowledge the leadership of the Jet Propulsion Laboratory who managed the GRAIL mission and also built the Ka-band inter-satellite ranging system that provided the data for measuring the lunar gravity.

References

[1] Zuber, M.T., Smith, D.E., Lehman, D.H., Hoffmann, T. L., Asmar, S.W., Watkins, M. M.: Gravity Recovery and Interior Laboratory (GRAIL): Mapping the Lunar Interior from Crust to Core, *Space Science Reviews* Journal, DOI 10.1007/s11214-012-9952-7

[2] Asmar, S.W. et al.: The Scientific Measurement System of the Gravity Recovery and Interior Laboratory (GRAIL) Mission, *Space Science Reviews* Journal, DOI 10.1007/s11214-013-9962-0

[3] Klipstein, W.M., et al.: The Lunar Gravity Ranging System for the Gravity Recovery and Interior Laboratory (GRAIL) Mission: *Space Science Reviews* Journal, DOI 10.1007/s11214-013-9973-x *Space Science Reviews* Journal, DOI 10.1007/s11214-013-9962-0

[4] Zuber, M.T., et al.; Gravity field of the Moon from the Gravity Recovery and Interior Laboratory (GRAIL) mission, *Science, 339,* doi: 10.1126/science.1231507, 2013.

[5] Wieczorek, M.A. et al.: The crust of the Moon, as seen by GRAIL, *Science, 340,* doi: 10.1126/science.1235768, 2013.

[6] Melosh, H.J., et al.: The origin of lunar mascon basins, *Science, 339,* doi: 10.1126/science.1231530, 2013.

[7] Williams, J.G., et al,: *J. Geophys. Res. Planets, 119*, 1546-1578

EPSC Abstracts
Vol. 12, EPSC2018-583, 2018
European Planetary Science Congress 2018

LROC: Nine Years Exploring the Moon

Mark Robinson (1) and LROC Team
(1) Arizona State University, Temp, AZ, USA (robinson@ser.asu.edu)

Abstract

The Lunar Reconnaissance Orbiter Camera (LROC) acquired its first image of the Moon on 30 June 2009 and has since acquired over 1.6 million Narrow Angle Camera (NAC) images and over 600 thousand Wide Angle Camera (WAC) images (WAC nominal mapping began 1 January 2010). LRO was originally intended to support a human return to the Moon by providing technical data for mission planning acquired over a one year period. After successfully meeting those exploration goals the spacecraft was given a new two year science focused mission. Subsequently three extended science missions were funded and valuable science data is still being returned (3rd extended mission). Thus far the LROC team members have contributed to at least 100 peer-reviewed LROC-observation based publications.

1. Introduction

The NAC has provided globally distributed coverage (>90% of the surface) at the meter scale and high science value targets have been observed under a broad range of temporal, lighting and viewing conditions allowing 2 to 5 meter scale topography, landform analysis, and albedo characterization. Major NAC based discoveries are broadly grouped into the fields of tectonism, volcanism, and impact cratering. The WAC has acquired over 100 nearly global 7-color datasets, each with unique lighting and viewing geometry providing the most comprehensive non-terrestrial global photometric dataset ever collected. Orbit-to-orbit overlap provides parallax measurements from which a global topographic model was derived for characterizing large-scale landforms and allowing pixel-by-pixel viewing and lighting angles.

1.1 Small Sampling of NAC Discoveries

LROC images have revealed globally distributed small-scale contractional tectonic landforms (>3500 lobate scarps) that were largely undetected prior to LRO. The pristine condition, crosscutting relations with small-diameter impact craters, and crater size frequency distribution dating all indicate a young age for the small lobate thrust fault scarps (<50 my). These young thrust faults provide a window into the recent stress state of the Moon and offer insights into the origin of global lunar stresses. The global distribution of the faults is evidence of a "shrinking Moon" from cooling of a still hot interior, and the pattern of the fault scarps is consistent with stresses from global contraction and superimposed tidal stresses. The young age of the fault scarps raises the possibility that coseismic slip events on the developing faults were recorded by the Apollo Seismic Network. Modelling of the current lunar stress state indicates that peak stresses are reached at apogee, and many of the recorded shallow moonquakes in proximity to scarps occurred when the Moon was near apogee. The emerging conclusion from is that the Moon is still tectonically active. The search for evidence of very recent change on young tectonic landforms using temporal pairs of LROC NAC images may provide the best case for current tectonic activity.

The longevity of the LRO spacecraft enables temporal observations used to discover changes to the surface. Temporal image pairs consist of "before" and "after" images acquired under nearly identical lighting and viewing geometries. Systematic scanning of over 24,000 temporal pairs revealed over 400 newly formed impact craters. Before/after ratio images reveal previously unknown proximal and distal reflectance zones around the impact sites that provide insight into the crater formation process. In some cases, the distal reflectance zones affect areas 100s of crater diameters away from the new crater. We infer that these broad surface disturbances are caused by vapour and melt that was jetted from the impact site soon after the bolide contacted the surface. Additionally, the temporal pairs revealed over 120,000 other surface changes termed "splotches". While some of the splotches may be small primary impact craters, clusters of splotches identified around newly formed craters suggest that many splotches are the result of secondary impacts. Continued collection and analysis of temporal observations during the

Cornerstone Mission will help refine the current impact rate and provide more insight into the cratering process and churning of the upper regolith caused by secondary impacts.

Prior to LRO, the Compton-Belkovich Volcanic Complex (CBVC) was known only as an isolated, enigmatic, Th-rich anomaly, located on the northern farside. Narrow Angle Camera (NAC) images revealed the volcanic character of the anomaly and, coupled with data from Diviner, showed the CBVC to be rich in silica, making it an example of rare high-Si volcanism on the Moon. The CBVC occupies an area of roughly 25 x 35 km, centered at 61.1°N, 99.5°E. The complex is characterized by high reflectance and elevated topography, including domes and cone, some with steep slopes and abundant boulders. These volcanic features formed from viscous lava and occur around a central, irregular depression, likely a collapsed caldera associated with silicic pyroclastic activity. Moon Mineralogy Mapper spectra suggest this volcanic activity involved release of indigenous H_2O-rich volatiles. CSFD analysis constrains the volcanism to have occurred 3.5 billion years ago. The CBVC is unique among silicic volcanic localities on the Moon in its well-preserved morphologies and apparent H_2O-rich, silicic pyroclastic activity.

High resolution Apollo 15 photography revealed the presence of an enigmatic landform, known as Ina, thought to have formed through volcanic processes. Due to its small size (<3 km width) and inadequate observations, a definitive formation mechanism was elusive, and possibilities included effusive and explosive eruptions over a broad range of ages. LROC provided high resolution imaging with a variety of lighting conditions, and stereo-based topography allowing a reinvestigation of Ina. A significant finding from LROC was the discovery of similar deposits occurring in over 50 locations spanning from eastern Mare Tranquillitatis across a broad arc (2500 km) to the Gruithuisen Domes. Crater size–frequency distributions (CSFD, diameters ≥10 m) from Ina (and other similar deposits) were interpreted as indicating an eruption age of <100 My.

1.2 Small Sampling of WAC Discoveries

The origin of lunar light plains has long been debated, particularly since the return of Apollo 16 impact breccias. Conflicting relative age estimates and geologic context suggest all light plains are ejecta from the Orientale and Imbrium basins, many impact events, or even volcanic eruptions. In order to distinguish between the various origins of light plains deposits both at the local and global scale, a consistent global map of light plains was produced using WAC observations (morphology, albedo, topography). Results from the farside highlands suggest that the bulk of the light plains within 4 radii of the Orientale rim formed as a result of the Orientale basin-forming impact. It appears that the Imbrium basin displays a similar, though less pronounced, trend. Further, flow features identified among light plains deposits during the creation of the global map preserve a record of the emplacement dynamics of light plains deposits and may provide critical insight into the physical properties of light plains and, therefore, the basin formation process.

Enigmatic albedo patterns known as swirls occur in many locations on the Moon but are not known to exist on any other Solar System body. The WAC ultraviolet bands provided the means to better map their distribution and extent. Swirls were distinguished as low 321/415 nm ratio coupled with moderate to high reflectance, with high optical maturity (OMAT) values, stronger 1-μm bands, and shallower normalized continuum slopes than their surroundings. This new comparison showed the swirls to be significantly more extensive than previously known and likely the result of diminished space weathering rates from magnetic shielding.

The extensive photometric coverage provided by the WAC observations allowed the derivation of the first resolved map (30 km scale) of Hapke parameters for any body in the Solar System. Surprisingly the Hapke maps demonstrate decreased backscattering in the maria relative to the highlands (except 321 nm band), probably due to the higher content of both SMFe (submicron iron) and ilmenite in the interiors of back scattering agglutinates in the maria.

Acknowledgements

The NASA Goddard Space Flight Center (GSFC, Greenbelt MD, USA) designed, built and operates the LRO spacecraft and we thank them for their amazing efforts. Malin Space Science Systems (MSSS, San Diego CA, USA) designed and built the LROC imaging system. This abstract summarizes some of the work contained in over 100 team papers, thus the lack of references.

EPSC Abstracts
Vol. 12, EPSC2018-603-1, 2018
European Planetary Science Congress 2018

The Distribution of Antipodal Ejecta from the Tycho Impact: Observations and Models

D. A. Paige (1), I. S. Curren (2), P. S. Russell (1), S. Moon (1), and A. K. Boyd (3)
(1) Dept. of Earth, Planetary, and Space Sciences, University of California Los Angeles, CA, 90095, USA (dap@moon.ucla.edu), (2) Weizmann Institute of Science, Rehovot, Israel (3) School of Earth and Space Exploration, Arizona State University, Tempe, AZ, USA

Abstract

LRO Diviner and LROC observations have previously revealed a ~100 km region of anomalous rock abundance and melt features in the antipodal region of the Tycho impact crater. Analysis of LROC WAC multi-color data reveals a much more widespread ~600 km concentration of antipodal Tycho ejecta that we interpret to be melt spherules that converged near the antipode on ballistic trajectories from the Tycho impact.

1. Introduction

The distribution of distal ejecta from major impacts is of broad interest for the field of planetary science. On Earth, the Chicxulub impact crater produced a global layer of ejecta that resulted in intense heating when it re-entered the Earth's atmosphere that may have resulted in extinction of the dinosaurs at the K/T boundary 65 million years ago [1,2]. On the Moon, the extensive ray system associated with the 108 million year old Tycho impact suggests that it also deposited an ejecta blanket of global scale, although the nature and effects of the Tycho impact may be less extensive as those from Chicxulub due to the Moon's lower gravity and Tycho's smaller size. Fortunately, the Moon's slow resurfacing rates have resulted preservation of a significant fraction of Tycho's ejecta on the lunar surface, and its distribution can be recognized in the LRO data with the aid of ballistic models.

2. Datasets and Methods

We used photometrically corrected LROC WAC mosaics in bands 1 (321 nm), 3 (415 nm) and 4 (566 nm) to create a false color map of the Tycho antipodal region at a spatial resolution of 65 pixels per degree (~475 m) [3]. We also use a 3-body ballistic model that includes the effects of lunar and Earth gravity, as well as the rotational and orbital motions of the moon to calculate the trajectories of Tycho ejecta at a range of azimuth and elevation angles as well as initial velocities See [1] and [4] for descriptions of analogous 2-body ballistic models.

3. Results

3.1 WAC Colour

The WAC color map reveals the presence of an extensive region with distinct UV spectral properties characteristic of glass and shocked plagioclase in the vicinity of the Tycho antipode [5], shown in purple in Figure 1.

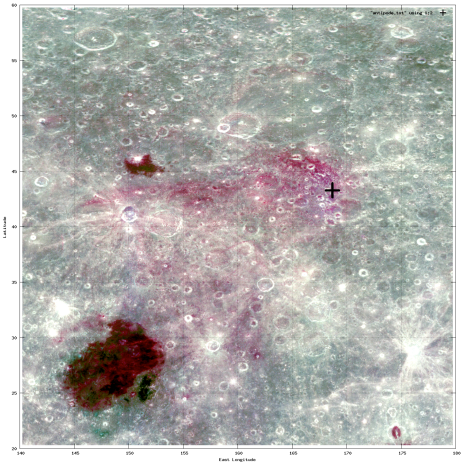

Figure 1. LROC WAC 3-band false color image of the Tycho antipodal region (extending from 140°E to 180°E and 20°N to 60°N). The location of the antipode is indicated by the black "+".

The purple areas in the false color map are concentrated to the south and to the east of the antipode. Areas with similar spectral features are also visible in the proximal rays of Tycho.

3.2 Ballistic Models

Ballistic model results predict a convergence of ejecta in the antipodal region for ejection angles of 0° to 45° relative to horizontal [6]. For increasingly higher ejection angles, the Moon's rotation results in the convergence of ejecta further to the west of the antipode point (Figures 2-4). The higher angle ejecta are distributed over a wider area to the west of the antipode with heating rates that are not sufficient to results in localized melting. Accumulations of small melt spherules, analogous to those that were deposited globally on Earth in association with Chicxulub, remain exposed on the surface and are responsible for the UV spectral features observed by LRO WAC. The convergence of low angle ejecta spherules just west of the antipode produces the most concentrated ejecta deposits, with re-impact heating rates sufficient to result in localized rubble formation, melting and flow features that are observed by LRO NAC and Diviner. [7-9].

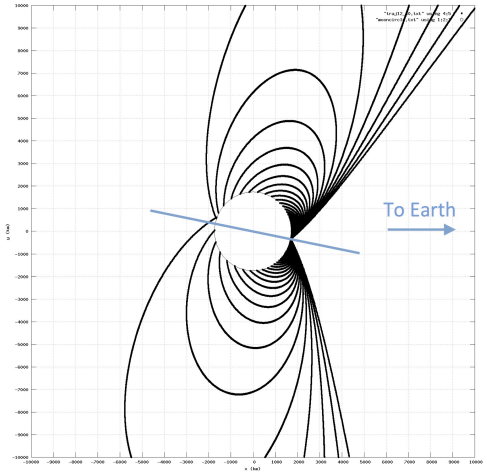

Figure 2. Ballistic models showing the trajectories of Tycho ejecta for ejection angles of 40°. The antipodal ejecta is concentrated to the west of the antipodal point due to the rotation of the Moon.

4. Conclusions

We conclude all the major observable global effects of the Tycho impact can be understood as a consequence of the ballistic emplacement of Tycho ejecta. Proximal rays, as well as widely distributed high-angle ejecta near the antipode are rich in spherules composed of glass and shocked plagioclase. Closer to the antipodal point, the convergence of low angle ejecta spherules became sufficiently intense as to initiate localized melting and flow. It is likely that antipodal deposits from major impacts are common on the Moon, but only the most recent deposits are detectable from orbit.

References

[1] Alvarez, W., Trajectories of ballistic ejecta from the Chicxulub Crater, in *The Cretaceious-Tertiary Event and Other Catastrophies in Earth History*, G. Ryder et al. editors, Spec. Pap. Geol. Soc. Am., 307, 141-250, 1996. **[2]** Kring, D. A., and D. D. Durda, Trajectories and distribution of the material ejected from the Chicxulub impact crater: Implications for postimpact wildfires, J. Geophys. Res. 107, E8, 5062 , 2002. **[3]** Boyd, A. K., Robinson, M. S. and H. Sato, Lunar Reconnaissance Orbiter Wide Angle Camera photometry: An empirical solution, 43d LPSC, Abstract 2795, 2012. **[4]** Dobrovolskis, A., Ejecta patterns diagnostic of planetary bodies, Icarus 47, 203-219, 2981. **[5]** Denevi, B. W, Robinson, M. S., Boyd, a. K., Sato, H. Hapke, B. W. and Hawke, B. R., Characterization of space weathering from Lunar Reconnaissance Orbiter ultraviolet observations of the Moon, J. Geophys. Res., Planets 10.1002/2013JE004527, 2013. **[6]** Jogi, P. and D. A. Paige, A ballistic model for antipodal impact melt deposits on the Moon, 45th LPSC, abstract #2574, 2014. **[7]** Robinson et al., An exceptional grouping of lunar highland smooth plains: Geography, morphology, and possible origins, Icarus 273, 121 (2016) **[8]** Bandfield, J. L., J. T. S. Cahill, L. M. Carter, C. D. Neish, G. W. Patterson, J.-P. Williams, Distal ejecta from lunar impacts: Extensive regions of rocky deposits, Icarus, 283, 282-299, 2017. **[9]** Curren, I. S., P. S Russell, D. A. Paige and s. Moon, Geologic evidence for impact ejecta origin of Tycho's antipode terrain, EPSC 2018 (this conference).

EPSC Abstracts
Vol. 12, EPSC2018-629, 2018
European Planetary Science Congress 2018

Investigating the Mandel'shtam lobate scarp complex

J. D. Clark (1), C. H. van der Bogert (2) H. Hiesinger (2) T. R. Watters (3) M. E. Banks (3, 4); (1) School of Earth and Space Exploration, Arizona State University, Tempe, AZ, USA (2) Institute für Planetologie, Westfälische Wilhelms-Universität, Münster, Germany (3) Center for Earth and Planetary Studies, National Air and Space Museum, Smithsonian Institution, Washington, DC, USA (4) NASA Goddard Space Flight Center, Greenbelt, MD, USA (jclark@ser.asu.edu)

Abstract

We performed crater size-frequency distribution (CSFD) measurements and determined absolute model ages (AMAs) for the scarps in the Mandel'shtam lobate thrust fault scarp complex. The scarps were determined to be late-Copernican in age, ranging from ~33 Ma to ~187 Ma. However, the crater population measured around the southern scarps in this complex may have been disturbed by crater ejecta from the Copernican-aged rayed Mandel'shtam F crater because the ages (around ~35 Ma) of these southern scarps are notably younger than other AMAs in the complex. We plan to perform CSFD measurements on the Mandel'shtam F crater ejecta to determine if the young scarp ages are the result of recent ejecta emplacement.

1. Introduction

Lobate scarps are the surface expression of low-angle thrust faults formed by contraction of the crust due to principally long-term interior cooling [1-6] and tidal deformation [7]. Lunar scarps are relatively small compared to most lobate scarps on other terrestrial planets (e.g., Mars and Mercury) and are typically <10 km in length and tens of meter in relief [3-5, 8-9].

Based on their crisp appearance and cross-cutting relationships with small-diameter (< 40 m) craters, lobate scarp are among the youngest landforms on the Moon [6, 10-12]. Lunar scarps typically occur in clusters often referred to as complexes [10]; these series may consist of several en echelon stepping scarps [8, 10].

Mandel'shtam Scarp Complex:

Located in the farside highlands, the Mandel'shtam lobate scarp complex (Fig. 1) is comprised of 8 distinct scarps with a total cumulative length of ~80 km. The complex's name derives from the close-by large Mandel'shtam craters, which range from ~ 25 to 60 km in diameter.

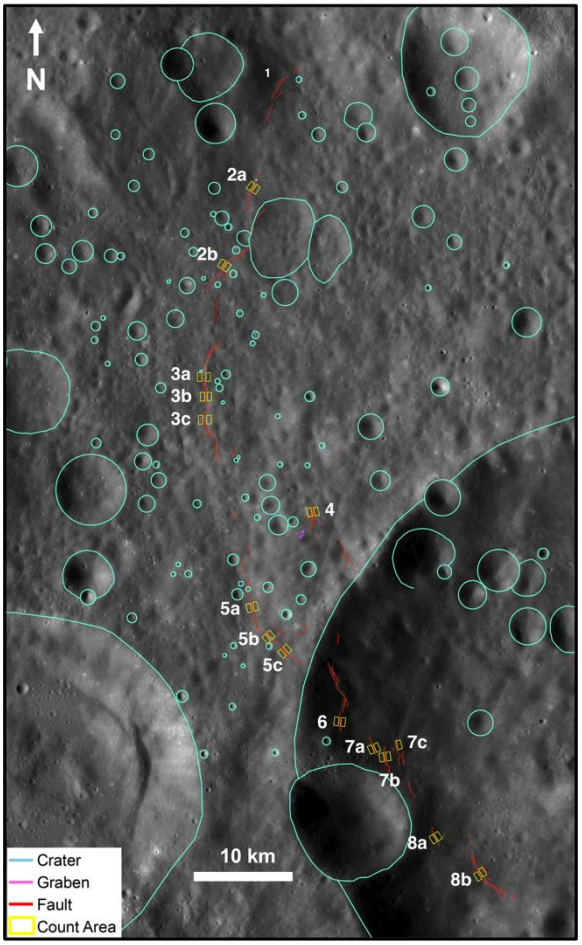

Figure 1: Simple structural map of the Mandel'shtam scarp complex (6.2°N, 161.2°E) displaying lobate scarps 1-8 (red lines) over a Lunar Reconnaissance Orbiter (LRO) Wide Angle Camera (WAC) mosaic. Count locations are mapped with yellow boxes and surrounding craters are mapped with an aqua outline.

Age determinations by [11] place the craters at Imbrian to pre-Nectarian in age (~3.5 to 4.2 Ga). Using crater degradation rates, [10] first determined ages for the scarps within the Mandel'shtam complex (Table 1). Individual scarp ages range from 100 ± 70 to 190 ± 70 Ma, with a calculated complex age of 180 ± 50 Ma [10]. Using more recent scarp dating

techniques, [12] and [13] determined the scarps within the complex to be ~ 33 Ma to 187 Ma, (Table 1). Comparing the ages for the individual scarps, we found that our ages were younger than those calculated by [10].

Table 1: List of ages for the lobate scarps within the Mandel'shtam scarp complex. (*) means an age was not determined due to inadequate image coverage or (**) because CSFDs were in equilibrium.

Scarp	Age (Ma) [10]	Age (Ma) [12-13]
1	170 ± 70	*
2	180 ± 60	
a		94 ± 8
b		146 ± 23
3	180 ± 50	
a		120 ± 9
b		100 ± 8
c		99 ± 8
4	100 ± 70	139 ± 15
5	190 ± 50	
a		**
b		187 ± 15
c		**
6	*	34 ± 4
7	180 ± 50	
a		36 ± 5
b		33 ± 4
c		125 ± 17
8	190 ± 70	
a		39 ± 11
b		87 ± 7

By dating individual scarps within the complex, we wanted to assess if there was an order to the development of the fault complex. Scarp 5 in the middle of the complex was determined to be the oldest or the scarp that ceased fault activity longest ago. Comparing the ages in the complex, there appears to be no clear trend of scarps becoming progressively younger towards the north or south terminus of the complex. We did, however, find that scarps 6-8 in the southern portion of the complex shared similar ages of ~34 Ma to ~39 Ma (yellow box in Fig. 2; Table 1).

Upon further inspection, an ejecta ray from Mandel'shtam F crater that appears blue in the Clementine color-ratio mosaic covers the southern area of the scarp complex (Fig. 2, yellow box).

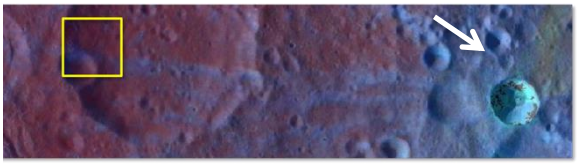

Figure 2: Clementine color-ratio image showing the 15 km-wide Mandel'shtam F crater in the east (indicated with white arrow) and scarps 6-8 in the west (yellow box).

We speculate that the cluster of ages of around 35 Ma might reflect an age for the crater and not the timing of the most recent fault activity.

2. Future Investigation

In order to determine an age for the Mandel'shtam F crater, we will conduct CSFD measurements on the crater ejecta, using LROC high-resolution Narrow Angle Camera (NAC) images. Conducting CSFD measurements on the ejecta blankets of Copernican-aged craters is a typical procedure because the crater floor units might give younger apparent ages due to target property effects [14, 15]. Additionally, we will date the surfaces distal to the scarp trace to investigate the extent and severity of seismic activity on the faults, and investigate the regional geology to provide context for the scarp measurements [13, 16]

3. Summary and Outlook

With CSFD measurements on the Mandel'stham F ejecta, we hope to determine the age of the crater and to resolve if the scarps' surfaces in the southern portion of the Mandel'shtam complex were last altered by fault activity, ejecta emplacement, or by other resurfacing processes.

References

[1]Schultz, P.H. (1976) Moon Morphology, University of Texas Press, Austin, TX. [2]Binder, A.B. (1982) *Earth, Moon, and Planets*, 26, 117-133. [3]Watters, T.R. (2003) *JGR.*, 108. [4]Watters, T.R. et al., (2009) *EPSL* 285, 285-296. [5]Watters, T.R. and Schultz, R.A. (2010) Planetary Tectonics, Cambridge Univ. Press. [6]Watters, T.R. et al., (2010) *Science*, 936-940. [7]Watters et al (2015) *Geology* 43, 851. [8]Watters, T.R. and Johnson, C.L. (2010) *Planetary Tectonics*, Cambridge Univ. Press, pp. 121-182. [9]Banks, M.E. et al., (2012) *JGR*,117,.[10]Binder A.B. and Gunga H. (1985) *Icarus*, 63, 421. [11]van der Bogert C.H. et al. (2012) *LPSC XLIII*, Abstract #1847. [12]Clark et al. (2015) *LPSC XLVI*, Abstract #1730. [13]van der Bogert et al. (2018) Icarus 306, 225-242 [14] Hiesinger et al. (2012) *JGR*117, E00H10. [15]van der Bogert et al (2017) *Icarus* 298, 49-63. [16]Clark et al. (2018) *LPSC XLIX*, Abstract #2692.

EPSC Abstracts
Vol. 12, EPSC2018-638, 2018
European Planetary Science Congress 2018

Effects of Visible Albedo on Mid-Infrared Spectra under Simulated Lunar Environment as Compared to Diviner Lunar Radiometer

Katherine Shirley and Timothy Glotch
Stony Brook University, New York, USA, (katherine.shirley@stonybrook.edu)

Abstract

Effects of space weathering on the mid-infrared have been shown to be present in the Diviner Lunar Radiometer Experiment dataset, and the decrease in visible albedo as a result of space weathering correlates well with the variations observed in the lunar mid-infrared data. In this study, we examine several locations on the Moon with variable degrees of space weathering to further examine this effect and compare the remote sensing data to laboratory spectra measured under simulated lunar environment conditions. We show that both laboratory and remote sensing spectra show similar trends of decreasing visible albedo with Christiansen feature values moving to longer wavelengths, and that the lunar locations examined show similar variation in Christiansen feature shifts corresponding to the type of feature, i.e. young craters versus swirls.

1. Introduction

Reduced visible albedo an optical effect of exposure to space weathering. While space weathering produces a number of physical changes to regolith on the Moon (vitrification, formation of nanophase iron rims, formation of agglutinates, and physical breakdown of regolith), the overall darkening of the regolith appears to be a driving factor in variation of mid-infrared spectral features [1].

Work by [2] noted that space weathering is apparent in the Diviner dataset, which targets the mid-infrared, and, specifically, the Christiansen Feature (CF). The CF is an emissivity maximum the corresponds to silicate polymerization and is used by Diviner to determine bulk silicate composition across the lunar surface. [3] developed an empirical correction to the Diviner CF dataset to account for variation due to space weathering by using an optical maturity parameter [4], and noted the anticorrelation between CF position and albedo. From laboratory work using a simulated lunar environment, we see similar shifts in the CF position in Apollo samples [5] and experimentally space weathered samples [1] to longer wavelengths with higher degrees of optical maturity or reduced visible albedo. Here we examine the utility of laboratory data from [1] to inform interpretation of Diviner data, and look at young lunar craters and swirls to understand differences in the albedo-CF correlation due to the mode of space weathering at these different types of features.

2. Study Sites

We expect to see the most variation in space weathering or optical maturity on the lunar surface at young craters that excavate fresh un-weathered material, and at swirls which are thought to dampen the solar and cosmic irradiation aspect of space weathering. From the optical maturity map [4], we chose Giordano Bruno Crater (36° N, 103° E), Kepler Crater (8° N, 38° W), Reiner Gamma Swirl (7.5° N, 59° W), and Airy Swirl (18° N, 5° E). These are all within relatively consistent surrounding terrain, and show the two types in a highlands (Giordano Bruno and Airy) setting, and in mare (Kepler and Reiner Gamma). Data from Kaguya Multiband Imager, Clementine and Diviner were used to measure albedo at 750 nm, optical maturity index, and CF value, respectively, at all of these locations.

3. Results

At all locations we observed the anticorrelation between visible albedo at 750 nm and CF value where decreasing albedo (increasing optical maturity) corresponds to CF values moving to longer wavelengths. Fig.1a shows Diviner and Kaguya maps

of Kepler Crater and Fig.1b the data for a profile taken from the crater to the surrounding material.

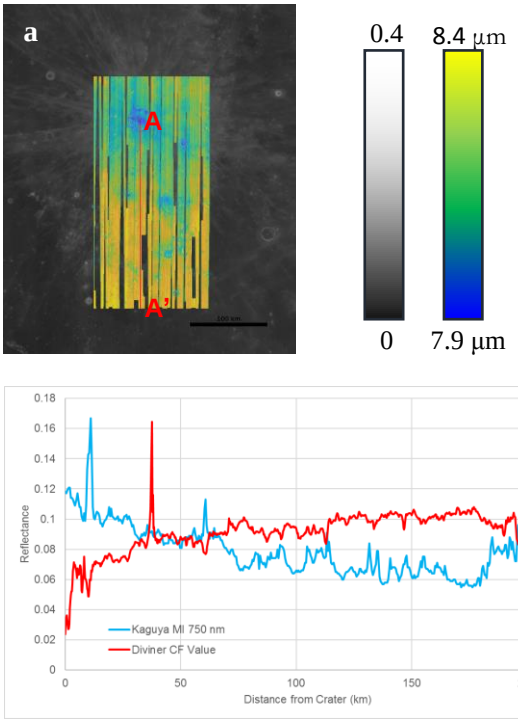

Figure 1: (a) Kepler Crater with Diviner CF value map (color) overlain on the Kaguya 750 nm reflectance (greyscale). (b) Data from A to A' for the Diviner CF value (red) and Kaguya 750 nm reflectance (blue) along the profile shown in (a).

4. Discussion and Conclusions

When directly comparing changes in albedo to those in CF value, we see linear trends in both the laboratory spectra and in the remote sensing data. When comparing the two (Fig.2) we see a much steeper trend in the laboratory data likely because we used anorthite which is brighter and purer than what we would find on the Moon and could therefore represent an endmember case. We see this further in the change in slope between the highlands and mare craters. The swirls show similar overall trends, but the linear trend is much weaker, which makes sense as the space weathering is different at the swirls than the craters. Overall we have shown similar trends in laboratory and remote sensing data and will include more sites and larger laboratory sets to better constrain the trends, and create a laboratory based calibration.

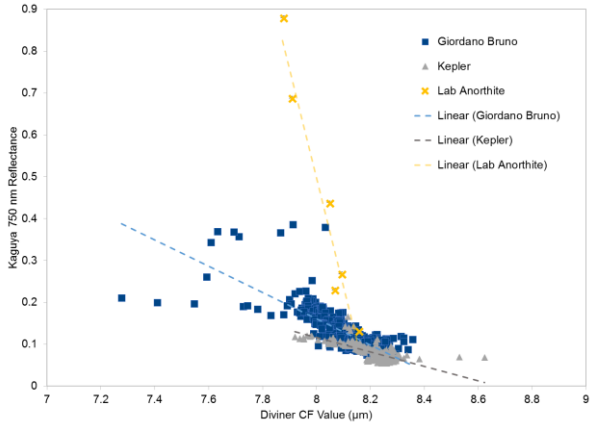

Figure 2: 750 nm albedo compared to CF values for Giordano Bruno Crater (blue squares), Kepler Crater (grey triangles), and laboratory measured anorthite (yellow Xs). All show linear trends of CF values moving to longer wavelengths with decreasing albedo, though with varying slope of those trends.

References

[1] Shirley, K. A., Glotch, T. D., Yang, Y., Jiang, T., & Zhang, H.: Synthetic Space Weathering Effects in the Near-and Mid-Infrared. In Lunar and Planetary Science Conference (Vol. 48). March 2017.

[2] Lucey, P. G., Paige, D. A., Greenhagen, B. T., Bandfield, J. L., & Glotch, T. D.: Comparison of Diviner Christiansen Feature position and visible albedo: Composition and space weathering implications. In Lunar and Planetary Science Conference (Vol. 41, p. 1600), March 2010.

[3] Lucey, P. G., Greenhagen, B. T., Song, E., Arnold, J. A., Lemelin, M., Hanna, K. D., ... & Paige, D. A.: Space weathering effects in Diviner Lunar Radiometer multispectral infrared measurements of the lunar Christiansen Feature: Characteristics and mitigation. Icarus, 283, 343-351, 2017.

[4] Lucey, P. G., Blewett, D. T., Taylor, G. J., & Hawke, B. R.: Imaging of lunar surface maturity. Journal of Geophysical Research: Planets, 105(E8), 20377-20386, 2010

[5] Hanna, K. D., Greenhagen, B. T., Patterson III, W. R., Pieters, C. M., Mustard, J. F., Bowles, N. E., ... & Thompson, C.: Effects of varying environmental conditions on emissivity spectra of bulk lunar soils: Application to Diviner thermal infrared observations of the Moon. Icarus, 283, 326-342, 2017.

EPSC Abstracts
Vol. 12, EPSC2018-646-1, 2018
European Planetary Science Congress 2018

Integrating Near and Thermal Infrared Data to Search for Lunar Mantle

R. Klima (1), J. Bretzfelder (1,2) D. Buczkowski (1), C. Ernst (1), B. Greenhagen (1), and N. Petro (3)
(1) Johns Hopkins University Applied Physics Laboratory, Laurel, MD, USA; (2) University of Southern California, Los Angeles, CA; (3) NASA/Goddard Space Flight Center, Greenbelt, MD, USA. (Rachel.Klima@jhuapl.edu / Fax: +1-443-778-8939

Abstract

Lunar missions in the last decade and the advancement of sample analysis techniques have resulted in a wealth of new information about the lunar surface. Integration of data across different subdisciplines is critical for addressing the outstanding science and exploration questions and identifying, as a community, what missions or advances would conclusively answer such questions. Recent studies [e.g., 1, 2], have shown the strength of integrating different remote sensing data sets with one another, or with sample studies. We here focus on a joint analysis using data from the Moon Mineralogy Mapper and the Diviner Lunar Radiometer.

1. Introduction

As an early crystallizing mineral, orthopyroxene provides important clues for understanding the evolution of the lunar surface, from the earliest magma ocean cumulates, through the anorthositic flotation crust, to later stage intrusive magmatism. Using data from the Moon Mineralogy Mapper (M^3) to search for Mg-suite norites, concentrations of low-Ca, high-Mg pyroxene have been characterized around the Imbrium and Apollo Basins [3]. These deposits may be exposures of Mg-suite plutons, may represent excavated material from deeper within the primary lower crust or mantle, or may be remnants of melt sheets (differentiated or undifferentiated). Iron-rich orthopyroxenes have been identified elsewhere, in smaller craters throughout the highlands crust.

The Imbrium basin has been extensively studied for many years [e.g., 4-5]. Though the bulk of the basin is flooded by mare basalts, massifs consisting of more generally feldspathic material surround the edges of Mare Imbrium in the northwest, northeast, and southeast (Fig. 1). Telescopic measurements of Apennine mountains revealed regions spectrally dominated by orthopyroxene or pigeonite [5]. Later radiative transfer modeling of Clementine data suggested that Mg-suite-like norites may surround much of the Imbrium basin [6]. In the initial global survey of norites using M^3 data, the norites modeled to have the highest Mg# were found in the Montes Alpes region near Vallis Alpes [3].

The Imbrium basin is large enough to have excavated between 60-85 km into the Moon [5], deep enough to penetrate through the crust and into the mantle. It is also associated with the strongest thorium detections by Lunar Prospector [7], and is likely to be rich in KREEP [8].

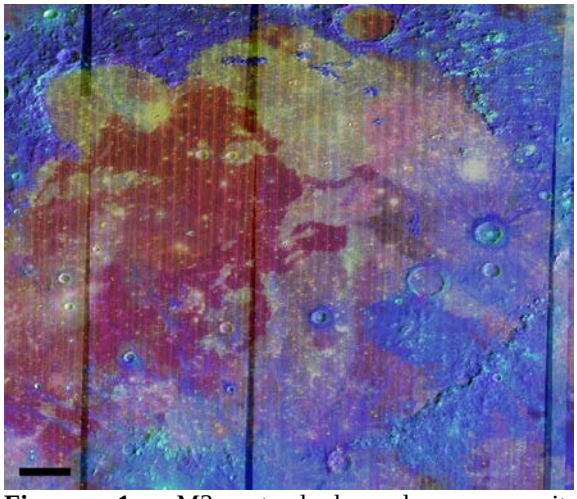

Figure 1: M3 standard color composite (R=integrated 1 μm band depth, G=integrated 2 μm band depth, B=1.58 μm reflectance). Orthopyroxene-rich regions appear as cyan. The highest concentration of Mg-rich orthopyroxene is in the massifs of Montes Alpes (NE corner). The center of Imbrium basin is located at 32.8°N 15.6°W and the scale bar is 100 km across.

2. Searching for Lunar Mantle

The Moon has experienced over a dozen impacts resulting in basins large enough to have excavated mantle material. With many of those basins

concentrated on the lunar near side, and extensive regolith mixing since the lunar magma ocean crystallized, one might expect that some mantle material would have been found among the lunar samples on Earth. However, so far, only a small number of candidate mantle samples [e.g. 9] have been identified, and their provenance is still debatable [10].

From orbit, a number of olivine-bearing localities, potentially sourced from the mantle, have been identified around impact basins [11]. Based on analysis of near-infrared (NIR) and imaging data, Ohtake et al. [12] suggest that roughly 60% of these sites represent olivine from the mantle. If this is the case and the blocks are coherent and not extensively mixed into the regolith, these deposits should be ultramafic, containing olivine and/or pyroxenes and little to no plagioclase. In the mid-infrared, they would thus exhibit Christiansen features (CF) at wavelengths in excess of ~8.5 μm, which has not been observed in global studies using Diviner [13].

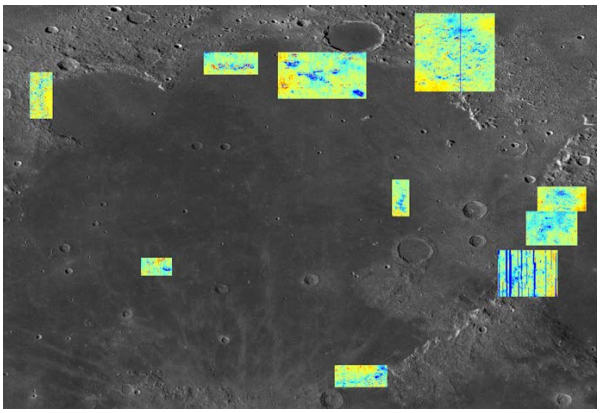

Figure 2: Diviner sites analyzed around Mare Imbrium. Low CF values (cool colors), consistent with anorthosite-dominated lithologies, while higher CF values (warm colors) are found among the mare deposits and in some of the massifs.

We are in conducting an integrated study of the massifs surrounding the Imbrium basin, which, at over 1000 km wide, is large enough to have penetrated through the lunar crust and into the mantle. These massifs are clearly associated with the Imbrium basin-forming impact, but existing geological maps do not distinguish between whether they are likely ejecta or rather uplifted from beneath the surface during crustal rebound [14]. We examine these massifs using visible, NIR and Mid-IR data to xdetermine the relationships between and the bulk mineralogy of local lithologies. Locations where Mid-IR data have been so far obtained are shown in Fig. 2. NIR data suggest that the massifs contain exposures of four dominant minerals: olivine, Mg-rich orthopyroxene, a second low-Ca pyroxene, and anorthite. Mid-IR results suggest that in the Montes Alpes region, the Mg-rich mafic material is present with substantial amounts of plagioclase. However, in the southeastern porting of Mare Imbrium, near Wolff Mons, the higher (~8.15 μm) CF values of these exposures suggest that these are more likely candidates for pyroxenite or very pyroxene-rich norite [15].

3. Conclusions and Future Work

For the specific example of our search for candidate mantle material on the lunar surface, integrated analyses suggest that perhaps the upper mantle is dominated by orthopyroxene instead of olivine. Analyses of these and other data sets will continue around Imbrium and other basins.

Acknowledgements

We are grateful to the NASA LDAP program for supporting this work under grant # NNX16AN50G and to the LRO project for support to N. Petro.

References

[1] Arnold, J. A., et al. (2016) *JGR* 121, 1342–61. [2] Crites, S. and Lucey, P., (2015) *Am. Min.* 100, 973. [3] Klima, R. L., et al. (2011), JGR, doi:10.1029 /2010JE003719. [4] Wilhelms D. E. et al. (1987), The geologic history of the moon, USGS, Washington, D.C.[5] Spudis, P., et al., (1988), LPSC XVIII, 155. [6] Lucey, P. G. and J. T. S. Cahill (2009), LPSC XL, #2424. [7] Lawrence, D. J. et al. (1998), Science, 281, 1484-1489. [8] Jolliff et al. (2000), JGR, 105, 4197. [9] Schmitt, H. H. (2016), *LPSC* 47, Abstract #2339. [10] Shearer, C. K. et al., (2015), *MAPS* 50, 1449. [11] Yamamoto et al. (2012) *GRL* 39, L13201. [12] Ohtake et al. (2017) *New Views of the Moon 2 – Europe*, Abstract #6016 [13] Greenhagen et al. (2010) *Science* 329, 1507. [14] Wilhelms D. E. et al. (1987), *USGS* Lunar map. [15] Bretzfelder, J. M. et al., (2018), *LPSC* 49, Abstract #1675.

EPSC Abstracts
Vol. 12, EPSC2018-748, 2018
European Planetary Science Congress 2018

Geologic Evidence for an Impact Ejecta Origin of Tycho's Antipode Terrain

I. S. Curren (1), P. S. Russell (2), D. A. Paige (2), and S. Moon (2)
(1) Weizmann Institute of Science, Rehovot, Israel, (*ivy.curren@weizmann.ac.il*) (2) University of California, Los Angeles, USA

Abstract

A region roughly antipode to the lunar crater Tycho exhibits anomalous melt geomorphologies and rock abundance characteristics. Although previous LROC and LRO Diviner observations cautiously link its origin to the Tycho impact and ballistic models demonstrate that antipodal ejecta focusing is possible, uncertainties remain regarding the plausibility of this formation mechanism. A multi-dataset analysis of the geomorphologies and terrain distributions located within Tycho's antipode region implicates the Tycho impact in the formation of this unusual deposit.

1. Introduction

Terrains with compositional or physical anomalies antipode to sizeable craters have been contentiously hypothesized to form by the convergence of seismic waves or airborne ejecta from the crater-forming impact [1-4]. The formation mechanisms should leave unique geomorphologic and spatial signatures [1], which may be detectable with remote sensing.

In this contribution, we analyze one such irregular region located on the lunar farside antipode to Tycho crater. The deposit exhibits smooth, formerly molten morphologies [5] and high rock abundances like those typically detected at Copernican-aged impacts [6]. The distribution of rock abundance within the region suggests that the material converged from a distal location [6] and crater counting places melts concurrent with the Tycho impact [7]. Global ballistic ejecta models demonstrate that material leaving Tycho could reach the antipode within hours leading to the emplacement of semi-viscid lava bombs [3] or particulate "rain" that becomes molten by frictional heating upon reimpact [8].

2. Methods and Datasets

Four distinct morphologies have been identified at Tycho's antipode: ponds, veneer, rock fences and rubble [5,8]. We use LRO NAC images to evaluate and map each of these morphologies on an individual basis. ArcGIS and Global Mapper software is then used to integrate NAC image analyses with Diviner Rock Abundance [6] and H-parameter maps [9], the WAC global color dataset, and SELENE DEMs. By employing a multi-scale and -dataset approach, we can preserve important morphological details while investigating regional scale relationships of the features to one another, and to underlying topography.

3. Results

3.1 Morphologic Analysis

Careful inspection of LROC NAC images reveals several new details regarding the four morphologies of the Tycho antipode region. The smooth pond morphology is seen to extend further toward the west than previously thought [5] in an elongate tail (Fig. 1), which is not unlike deposit geometry predicted from ballistic modeling [1,8]. Comparing pond and enclosing drainage area diameters shows that small craters fill more so than large ones, suggesting a regionally uniform emplacement consistent with the ballistic particulate "rain" hypothesis. We find no morphological evidence of meter-scale or larger molten ejecta blobs striking the surface [3].

At convex slopes in thick veneer flows where rock fences tend to form, we observe instances of detached boulders lying above smooth veneer or ponds. The superposition of these features indicates the occurrence of post-emplacement modification. The "weird terrain" on Mercury has been proposed to have formed as a result of the convergence of seismic waves from its antipodal crater [2]; although our tumbling boulders could be an outcome of shaking, we do not think this is the case here, as seismic waves should arrive more quickly than melt ponds could cool. A size-frequency distribution of boulders gives a mean diameter (~ 6m) that suggests veneer deposits may be thicker than previously reported [5].

We also noted several instances of "pond breakouts," locations where depressions spill out into an adjacent depression. The fronts of breakouts frequently exhibit morphology akin to ropy pahoehoe lava flows on Earth [10]. To achieve viscosities of terrestrial pahoehoe, lunar highlands anorthosites would require temperatures over 1500 K [11]. Using a reasonable pahoehoe viscosity as a baseline, the known flow distance and slope from the SELENE dataset, and a minimum flow thickness of 1 m, we calculate that material must accumulate rapidly (on the scale of hours) for the ejecta "rain" scenario to be plausible.

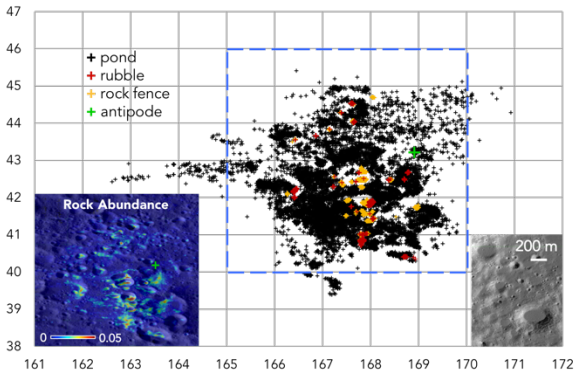

Figure 1: Distribution of morphological features at Tycho's antipode. Ponds (right inset) are the most common feature in the region. Rock abundance map (left inset) of the dashed blue box is ~100 km wide.

3.2 Integrated Dataset Analysis

Results from the GIS portion of our study show that Tycho's antipode terrain is apparent not only in high-resolution NAC images, but also at the regional scale in rock abundance, H-parameter, and WAC global color datasets. LRO Diviner rock abundance [6] and H-parameter [9] maps demonstrate the westward pointing chevron geometry of the deposit, consistent with our pond map and ballistic antipode ejecta models [1,8]. Several tails emanate outward from the main concentration of the deposit, bearing azimuths that mirror rays originating from Tycho. As in a previous study [6] we note the absence of high rock abundances on the S to SE-facing slopes of craters, which conveniently mirrors the shadow zone of Tycho's rays. Such shadow zones are thought to be a product of low angle (oblique) impacts, which in turn produce low angle (<45°) ejecta [12]. Low angle ejecta is required to form much of the high rock abundance signature found Tycho's antipode [6]. Finally, we find that the WAC color anomaly, which displays UV properties characteristic of glass and shocked plagioclase [13], covers a more diffuse area of Tycho's antipode than other datasets.

4. Summary and Conclusions

The Tycho antipode region exhibits terrains with unique geomorphologic and physical characteristics, which are apparent in multiple datasets. Detailed examination of the local and regional geology demonstrates that a ballistically emplaced antipode ejecta model consistent with particulate "rain" is plausible for the formation of the deposit. The recognition of these unique set of features as being linked with antipodal impacts will aid in future analysis of planetary surface and impact processes.

References

[1] Wieczorek, M.A. and Zuber, M.T.: A Serenitatis origin for the Imbrian grooves and South Pole-Aitken thorium anomaly, J. Geophys. Res., V. 106, E11, 2001. **[2]** Watts, A.W., Greeley, R., and Melosh, H.J.: The formation of terrains antipodal to major impacts, Icarus, V. 93, pp. 159–168, 1991. **[3]** Artemieva, N.A.: Tycho crater ejecta, 44th LPSC, 18-23 March 2013, Houston, TX. **[4]** Jögi, P., and Paige, D.P.: A Ballistic Model for Antipodal Impact Melt Deposits on the Moon, 45th LPSC, 17-21 March, 2014, Houston, TX. **[5]** Robinson M.S., Thomas, P.C., Plescia, J.B., et al.: An exceptional grouping of lunar highland smooth plains: Geography, morphology, and possible origins, Icarus, V. 273, pp. 121-134, 2016. **[6]** Bandfield, J.L., Cahill, J.T.S., Carter, L.M., et al.: Distal ejecta from lunar impacts: Extensive regions of rocky deposits, Icarus, V. 283, pp. 282-299, 2017. **[7]** Williams, J.-P., Paige, D.A., and Jögi, P.: Impact Melt Deposits at the Antipodes of Tycho and Copernicus Craters, 46th LPSC, 16-20 March 2015, Houston, TX. **[8]** Curren, I.S., Paige, D.A., and Esturas, L.: An impact model for the origin of rocky surfaces and melt deposits at the antipode of Tycho crater, 47th LPSC, 21-25 March 2016, Houston, TX. **[9]** Hayne, P., Bandfield, J., Siegler, M., et al.: Global Regolith Thermophysical Properties of the Moon From the Diviner Lunar Radiometer Experiment, J. Geophys. Res.: Planets, V. 122, pp. 2371-2400, 2017. **[10]** Crown, D.A. and Baloga, S.M.: Pahoehoe toe dimensions, morphology, and branching relationships at Mauna Ulu, Kilauea Volcano, Hawai'i, Bull. Volcan., V. 61, pp. 288-305, 1999. **[11]** Handwerker, C.A, Onorato, P.I.K., and Uhlmann, D.R.: Viscous flow, crystal growth, and glass formation of highland and mare basalt from Luna 24, *in* Merill R.B. and Papike, J.J. (eds.), Mare Crisium: The View from Luna 24, pp. 483-493, Pergamon Press, New York, 1978. **[12]** Anderson, J.L.B., and Schultz, P.H.: Asymmetry of ejecta flow during oblique impacts using three-dimensional particle image velocimetry, J. Geophys. Res., V. 108, E8.

EPSC Abstracts
Vol. 12, EPSC2018-817, 2018
European Planetary Science Congress 2018

Lunar and Mercury morphometric crater catalogues (diameter 1-10 km)

N. Kozlova, M. Kolenkina, A. Zharkova, I. Zavyalov, A. Kokhanov, I. Karachevtseva
Moscow State University of Geodesy and Cartography (MIIGAiK), MIIGAiK Extraterrestrial Laboratory (MExLab), Moscow, Russia (n_kozlova@miigaik.ru)

Abstract

The work presents first results and future plans in creation of Lunar and Mercury crater catalogues for analysis of morphologic peculiarities of craters and comparative studies of extraterrestrial territories.

1. Introduction

The work is aimed at getting the new information about morphology of the Moon and Mercury via studying morphometric parameters of craters. We suppose that quantitative measurements of craters' characteristics will give new opportunities for comparative analysis of the Moon and Mercury.

2. Methods and Techniques

Generation of a morphometric catalogue can be presented in several steps.

First step is manual visual identification of craters using orthomosaics or/and DTMs. Assuming that the majority of craters have circle rim, we are trying to draw crater boundary at the highest points of the rim (Fig. 1). For this step we are using ArcGIS CraterTools software [1] and as a result we obtain a catalogue with position and diameters of craters.

Second step includes calculation of main morphometric parameters, such as maximum steepness on inner slopes and crater depth. To determine slope steepness we use DTMs and simple combination of ArcGIS functions. Measurement of depth is more challenging because it is highly influenced by relief of the surrounding surface. So we suggest using special program modules:

- d/D Calculation [2]
- CraMo [3]

These two modules are using different algorithms for calculation of crater depth, so they can complement each other and verify the results. Combining coordinate catalogue with computed parameters we obtain morphometric catalogue. However, automated measurements still work not for all craters. For craters which intersect or lay on each other, highly degradated craters, or craters located on inclined surface the algorithms may fail. So, not all craters with selected size have morphometric parameters in our catalogue. We are working to improve the technique for crater measurements.

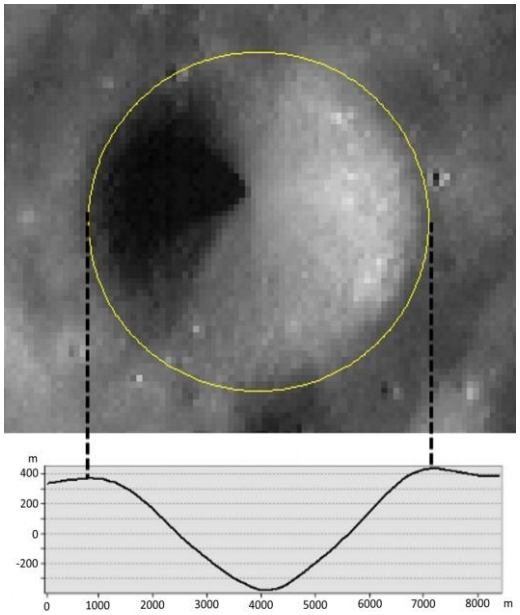

Figure 1: Visual identification of craters.

3. Lunar Crater Catalogue

We have completed global morphometric catalogue of Lunar craters 1-10 km in size which includes about 300 000 craters [4].

Crater identification was based on WAC_GLOBAL orthomosaic with pixel size 100 m. Morphometric parameters were determined based on DEMS with the same resolution: LDEM45 for polar areas and GLD100 for the rest parts. Such resolution of the

input data provided us opportunities to measure craters more than 1 km in diameter.

Such dataset can be used as an instrument for statistics and comparative studies, e.g. Fig. 2 presents depth to diameter ratio (d/D) for craters of studied diameters in some selected mare and highland regions. The graph shows that mare craters have typically higher depth to diameter ratio that is in agreement with theory of slower crater degradation rate in mares.

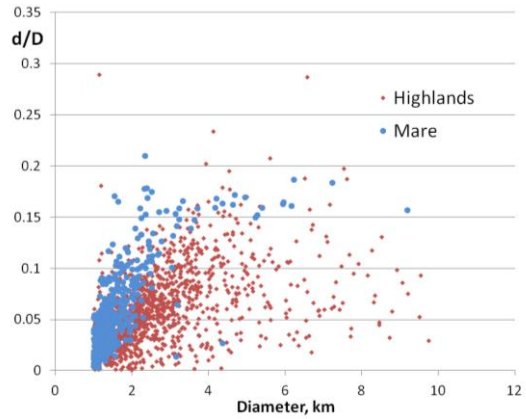

Figure 2: Depth to diameter ratio (d/D) for craters of studied diameters in mare and highland lunar regions.

4. Mercury Crater Catalogue

Existing global Mercury crater catalogue includes craters more than 10 km in size [5]. So in this study we aim to investigate craters less than 10 km.

To create Mercury morphometric catalogue we will use the newest data obtained by MESSENGER spacecraft, such as image mosaics and terrain models, created in 2017 and later, including:

- Global morphology mosaic with resolution 166 meters/pixel (http://messenger.jhuapl.edu/Explore/images/MESSENGER_Mosaics/Monochrome_Morphology_20170512_PDS16_equirectangular_thumb.png) produced from MESSENGER'S MDIS (Mercury Dual Imaging System) Wide Angle camera images.

- Global Mercury DEM with the resolution 665 m/pixel, obtained with the photogrammetric processing of the MESSENGER data [6].

- DTMs on Mercury quadrangles with resolution ~222 m/pixel and a vertical accuracy of about 30 m [7] based on photogrammetric processing of MESSENGER stereo images.

5. Summary and Conclusions

Study of large arrays of craters (ranging in size from 1 to 10 km) based on the morphometric catalogues of the Moon and Mercury will allow evaluation of differences and similarities between the endogenous and exogenous processes, crater morphology and degradation rate at the studied celestial bodies.

Acknowledgements

Creation of Lunar crater catalogue (1-10 km) was supported by Russian Foundation for Basic Research (RFBR), project No. 16-37-00323.

The works on Mercury crater catalogue and surface analysis are planned in the frame of Russian Science Foundation (RSF) project No 18-77-10053.

References

[1] Kneissl T., van Gasselt S., Neukum G., Map-projection-independent crater size-frequency determination in GIS environments – New software tool for ArcGIS, Planetary and Space Science, 59, 1243-1254, DOI: 10.1016/j.pss.2010.03.015, 2011.

[2] Kokhanov A.A., Bystrov A.Y., Kreslavsky M.A., Matveev E.V., Karachevtseva I.P. Automation of morphometric measurements for planetary surface analysis and cartography. Int. Arch. Photogramm. Remote Sens. Spatial Inf. Sci., XLI-B4, 431-433, doi:10.5194/isprs-archives-XLI-B4-431-2016, 2016.

[3] Kokhanov A.A., Kreslavsky M.A., Karachevtseva I.P. Small impact craters in the polar regions of the Moon: peculiarities of morphometric characteristics. Solar System Research. Vol. 49, No 5, pp. 295-302. (doi:10.1134/S0038094615050068), 2015.

[4] Kozlova N.A., Zavyalov I.Yu., Kolenkina M.M. Morphometric catalogue of lunar craters 1-10 km in diameter // The Eighth Moscow Solar System Symposium, Moscow, 9-13 October 2017.

[5] Fassett, C.I., S. J. Kadish, J. W. Head, S. C. Solomon, and R. G. Strom. The global population of large craters on Mercury and comparison with the Moon. Geophys. Res. Lett., 38, L10202, doi: 10.1029/2011GL047294, 2011.

[6] Becker, K.J., Robinson, M.S., Becker, T.L., Weller, L.A., Edmundson, K.L. Neumann, G.A., Perry, M.E., Solomon, S.C.: First Global Digital Elevation Model of Mercury, 47th Lunar and Planetary conference, The Woodlands, Texas, March 21-25, Abstract # 1903, 2016.

[7] Preusker, F. Oberst, J., Stark, A., Matz, K-D., Gwinner, K., Roatsch, T.:. High-Resolution Topography from MESSENGER Orbital Stereo Imaging – The Southern hemispehre, EPSC Abstracts, Vol. 11, EPSC2017-591, 2017.

EPSC Abstracts
Vol. 12, EPSC2018-1127-3, 2018
European Planetary Science Congress 2018

DEM generation and rover landing at the south pole of the Moon

Lang. Feng and Jan-Peter Muller

Imaging Group, Mullard Space Science Laboratory (MSSL), Department of Space & Climate Physics, University College London, Holmbury St Mary, Surrey, RH5 6NT, United Kingdom (lang.feng.14@ucl.ac.uk; j.muller@ucl.ac.uk)

Abstract

We describe the generation and fusion of digital topographic models (DTMs) derived from LROC NAC image via photogrammetry and LRO Mini-RF images (Stereo) via radargrammetry. Moreover, fast and automatic DTM co-registration with a LOLA DTM is studied for finding the correct and precise planned location for a safe planetary rover landing.

1. Introduction

Radar (radio detection and ranging) is currently one of the important research areas for Earth and moon observation and for helping human beings explore and search for organics on other planetary surfaces and their icy moons, many radar satellites have been or are about to be launched, such as Magellan (1994) radar for Venus, Cassini (1997) radar for Saturn's moons, Mars Reconnaissance Orbiter (2006) Shallow Radar (SHARAD) sounder and Mars Express (2004) Mars Advanced Radar for Subsurface and Ionosphere Sounding (MARSIS) for Mars, Lunar Reconnaissance Orbiter (LRO 2009) Miniature Radio Frequency (Mini-RF) for the Earth's moon and in the near future JUICE mission [1] (RIME - Radar for Icy Moons Exploration, SWI - Sub-millimeter Wave Instrument, RPWI - Radio & Plasma Wave Investigation, 3GM radio science package - Gravity & Geophysics of Jupiter and Galilean Moons) for Jupiter's moons. The Magellan multimode S band radar has three modes: SAR, altimetry, and passive radiometry to map almost all of the Venusian surface, whilst the Cassini RADAR instrument transmits and receives Ku-band micro-wave radiation, which operates in both passive (radiometer) and active (altimeter, SAR imaging, scatterometer) modes. Venera 15 and 16 radio occultation experiment data at Venus, Magellan stereo SAR data and Cassini RADAR data and Radio and Plasma Wave Science(RPWS) data are open to the scientific community through the PDS. Moreover, Lunar Reconnaissance Orbiter (LRO) Mini-RF data (S band and X band Raw data, Bistatic Radar data, Level 1 SAR, Level 1 interferometry, Level 2 SAR, Level 3 SAR mosaics, and Level 3 Sandia SAR Stereo data [2]) are available at PDS too, which will greatly advance our understanding of our moon, giving us a first look inside the Moon's coldest, permanently shadowed darkest polar craters with water ice.

2. DTMs generation using photo-grammetry & radargrammetry

For the moon, stereo radar images (LRO Mini-RF) and metadata are first prepared in ISIS. Then a rigorous sensor model (RD model) is developed. After co-registering the radar images as closely as possible to one another, stereo radar images, Bundle adjustment and dense matching is implemented for DTM production. The control points for the Moon are LOLA data. Meanwhile, the DEM is also generated by photogrammetry using LROC NAC stereo images, and then the two DEMs are fused to achieve a better DEM in the permanently shadowed polar region [3].

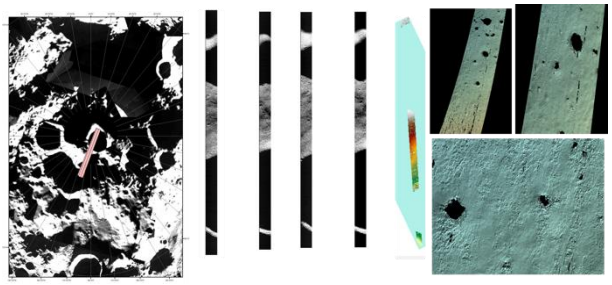

Figure 1: LRO LROC NAC image position, data, DEM result and close-up in DEM with colourmap

3. Fast and automatic DTM co-registration algorithm to improve

precise and safe planetary rover landing on planetary polar region.

DTM co-registration (the TRN algorithm) is studied, whether the DTM is generated by imaging, lidar or radar techniques within the landing equipment, for finding the correct and precise planned landing location for safe planetary rover landing.

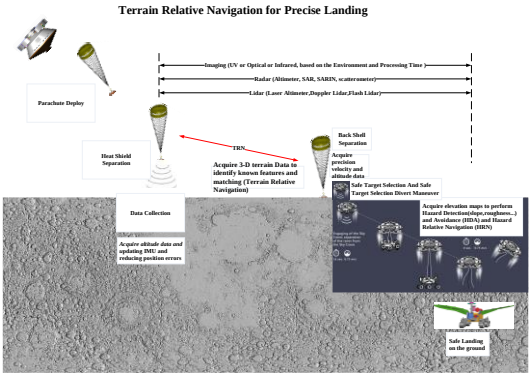

Figure 2: The timeline for a Terrain Relative Navigation for Precise Landing in the atmospheric environment of a celestial body (the red line) (DTM can be made by lidar, radar altimeter, stereo imaging and so on), note: When the landing environment has an atmosphere, like on Mars, a parachute can be used, if landing area has no atmosphere, like the Moon, thrusters are used instead of parachutes.

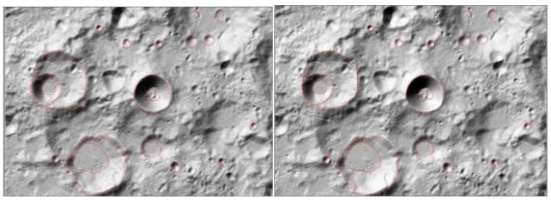

Figure 3: *DTM before and after co-registration at the south pole of the Moon*

4. Summary and Conclusions

In this paper, DEM generation and fusion via photogrammetry and radargrammetry are discussed, and a fast and automatic DTM co-registration algorithm (TRN) is presented, studied and tested for finding the correct landing site and precise and safe planetary rover landing. The Moon experiments demonstrate that the algorithm works very well for rover landing.

Acknowledgements

This work is partially supported by the CSC and UCL MAPS Dean prize through a PhD studentship at UCL-MSSL.

References

[1] Grasset, O., et al., *JUpiter ICy moons Explorer (JUICE): An ESA mission to orbit Ganymede and to characterise the Jupiter system.* Planetary and Space Science, 2013. **78**: p. 1-21.

[2] Raney, R.K., et al., *The lunar mini-RF radars: Hybrid polarimetric architecture and initial results.* Proceedings of the IEEE, 2011. **99**(5): p. 808-823.

[3] Rosiek, M., R. Kirk, and A. Howington-Kraus. *Lunar south pole topography derived from Clementine imagery*. in *New Views of the Moon 2: Understanding the Moon Through the Integration of Diverse Datasets*. 1999.

EPSC Abstracts
Vol. 12, EPSC2018-1208, 2018
European Planetary Science Congress 2018

South Pole-Aitken basin: outcrops and volcanic structures

Daniela Rommel[1], Arne Grumpe[1] and Christian Wöhler[1]

[1]Image Analysis Group, TU Dortmund University, Otto-Hahn-Str.4, 44227 Dortmund, Germany
(daniela.rommel@tu-dortmund.de)

Abstract

Since the South Pole-Aitken (SPA) basin is a large structure and has been exposed to subsequent impacts, the composition of SPA and its craters is of high importance for models of the lunar crust. We examined two interesting craters, namely Antoniadi and von Kárāman located inside SPA, which exhibit volcanic structures and patches of anorthosite-rich rock. Our analysis based on the Lunar Reconnaissance Orbiter Camera (LRO) Wide Angle Camera (WAC) mosaic [1] in combination with Narrow Angle Camera (NAC) [2] images for detailed views, and hyperspectral images of the Moon Mineralogy Mapper (M^3) [3] and topographic datasets of the GLD100 [4].

1. Introduction

The South Pole-Aitken (SPA) basin on the farside of the Moon has a diameter of more than 2500 km and was formed probably more than 4 Ga ago [5]. In our work, we investigate sections of the South Pole-Aitken basin (SPA), to gain insights and conclusions of the formation of the SPA. We analyse in detail the craters Antoniadi (Fig. 1) and von Kármán (Fig. 2) in order to study the appearance of anorthositic layers and volcanic constructs inside SPA.

2. Study of conspicuous structures

1.1 Antoniadi

The crater Antoniadi (138 km diameter, centered at 69° S, 173° W) is situated in the southern part of SPA (Fig. 1). Based on a petrological map constructed using the framework of [6], we investigated a large patch of anorthosite in the western part of the Antoniadi crater wall, covering a part of the outer crater floor not covered by lava. This deposit looks like an outcrop rather than a debris flow. Also the highest part of the gently inclined crater terrace show an anorthositic deposit, located exactly between the crater walls of Antoniadi and its neighbor Minnaert, which is partially superposed by the wall of Antoniadi. This anorthositic material was probably excavated by two subsequent large impacts.

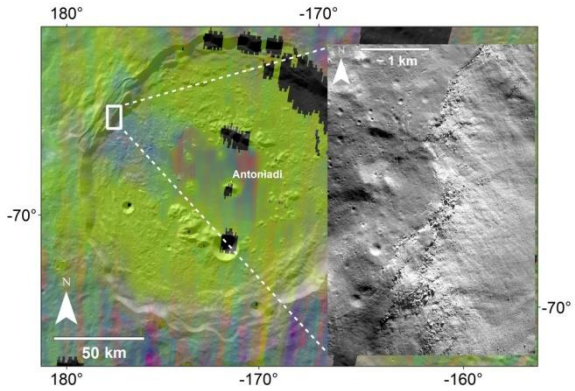

Fig. 1: Petrological map overlaid on LRO WAC mosaic of crater Antoniadi (red: basalt; green: Mg-rich rock; blue: anorthosite) with detail view of an anorthositic outcrop in the crater wall.

1.2 Von Kármán and von Kármán M

The crater von Kármán (186 km diameter, centred at 44° S, 176° E) is located in the inner region of the SPA basin (Fig. 2a). We investigate traces of basaltic volcanic activity in and around the crater von Kármán. The lava-flooded floor of von Kármán exhibits lobate flow structures of 16 x 33 km² size and 115 m height (Fig. 2b). On the lava-flooded floor of von Kármán M, a slightly elliptical dome structure of 15 x 17 km² size and 100 m height is situated (Fig. 2c). Both structures show sharp demarcations with respect to the underlying surface, indicated by white arrows in Fig. 2b and c. The occurrence of such presumably effusive volcanic structures in mare areas is commonly explained by lavas erupting in the

final phase of a long-lasting basaltic eruption, forming cooling-limited flows [7].

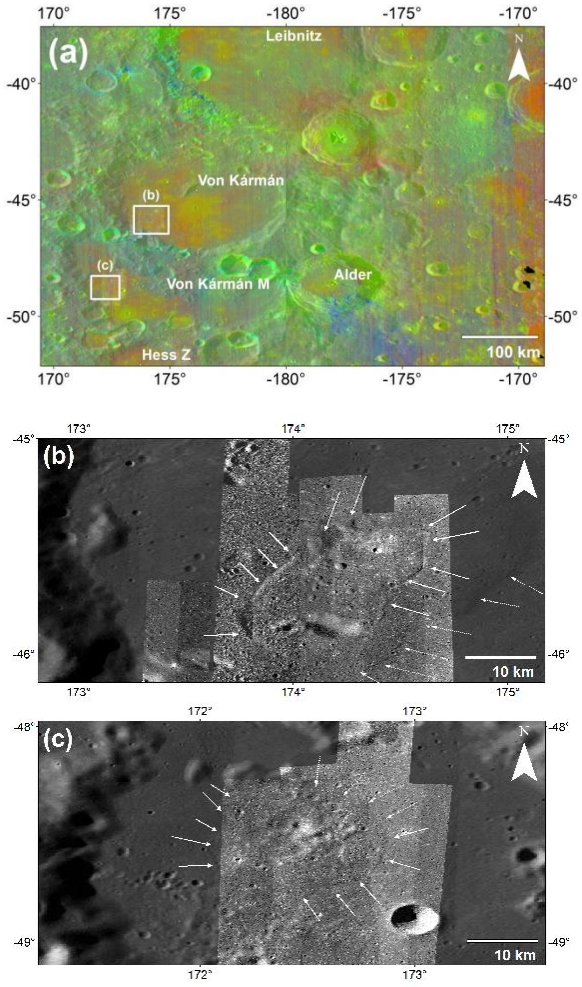

Fig. 2: (a) Petrological map overlaid on LRO WAC mosaic of the crater Von Kármán and von Kármán M (red: basalt; green: Mg-rich rock; blue: anorthosite). The white boxes show the position of the enlarged views. (b) LROC NAC image of the volcanic flow structure on the floor of von Kármán. White arrows indicate the outline of the structure (NAC images: M1110668243, M1174258554, M1183672804, M1102432165, M103375421). (c) LROC NAC image of the elliptical dome structure on the floor of von Kármán M. White arrows indicate the outline of the structure (NAC images: M1113033310, M182394642, M1204865030, M1250789112, M1174265624).

References

[1] Speyerer, E. J., Robinson, M. S., Denevi, B. W.: Lunar Reconnaissance Orbiter camera global morphological map of the Moon. Lunar Planet. Sci. XXXXII, abstract #2387, 2011.

[2] Robinson, M. S., and 22 coauthors: Lunar Reconnaissance Orbiter Camera (LROC) Instrument Overview. Space Sci. Rev., Vol. 150, No. 1-4, pp. 81-124, 2010.

[3] Pieters, C. M. and 19 coauthors: The Moon Mineralogy Mapper (M3) on Chandrayaan-1. Current Science, Vol. 96, No. 4, pp. 500-505, 2009.

[4] Scholten, F., Oberst, J., Matz, K.-D., Roatsch, T., Wählisch, M., Speyerer, E. J., Robinson, M. S.: GLD100: The near-global lunar 100 m raster DTM from LROC WAC stereo image data. J. Geophys. Res., Vol. 117, E00H17, 2012.

[5] Hurwitz, D. M. and Kring, D. A.: Differentiation of the South Pole-Aitken basin impact melt sheet: Implications for lunar exploration, J. Geophys. Res., Vol. 119, pp. 1110-1133, 2014.

[6] Wöhler, C., Grumpe, A., Berezhnoy, A., Bhatt, M. U., Mall, U.: Integrated topographic, photometric and spectral analysis of the lunar surface: Application to impact melt flows and ponds. Icarus, Vol. 235, pp. 86-122, 2014.

[7] Head, J. W. and Wilson, L.: Generation, ascent and eruption of magma on the Moon: New insights into source depths, magma supply, intrusions and effusive/explosive eruptions (Part 2: Predicted emplacement processes and observations), Icarus, Vol. 283, pp. 176-233, 2017.

EPSC Abstracts
Vol. 12, EPSC2018-1286, 2018
European Planetary Science Congress 2018

LROC Narrow Angle Camera Photometric Analysis of Crustal Lithologies: Pure Anorthosite Locales

Brad Jolliff (1), Ryan Watkins (2), Anna Schonwald (1), Timothy Hahn (1), and the LROC Science Team (3)
(1) Washington University in St. Louis, Missouri, USA, (2) Planetary Science Institute, Tucson, Arizona, USA, (3) Arizona State University, Tempe, Arizona, USA (bjolliff@wustl.edu)

Abstract

LROC NAC images coupled with digital topographic data derived from NAC geometric stereo image sets provide a powerful tool to assess compositional and surface property variations at a high spatial resolution. We use Hapke photometric modeling, incorporating local variations in illumination geometry, to derive single scattering albedo. We then assess local variations in albedo to explore the makeup and properties of regolith at a suspected purest-anorthosite locale in the Inner Rook Ring of Orientale basin.

1. Background

Many geologic questions can be addressed with the Lunar Reconnaissance Orbiter Camera (LROC) Narrow Angle Camera (NAC) images, 0.5 m per pixel (mpp) at an orbital altitude of 50 km. In this work, we investigate areas that have been identified as sources of highly pure anorthosite (purest anorthosite or PAN [1] (plagioclase > 98%)) on the basis of NIR spectral reflectance data. We combine NAC images with digital terrain models (DTMs [2]) derived from NAC geometric stereo images (i.e., two different sets of NAC image pairs taken of the same terrain on subsequent orbits with slightly different viewing angles), to compute local slopes and viewing geometry. We then derive the single scattering albedo (*w*), at ~NAC DTM resolution, using a Hapke photometric model [3,4,5]. With this approach, Watkins et al. [4] found that by taking local slopes and illumination geometry into account (i.e., normalizing for illumination geometry at the pixel scale), variations in reflectance are primarily affected by (1) maturity, and (2) composition. Then, by comparing soils of similar maturity (submature to mature), reflectance was shown to correlate well with composition, namely with the ratio of feldspathic to mafic contents. Watkins et al. [4] used Apollo landing site data to demonstrate this relationship, and Hahn et al. [5] demonstrated the correlation using Apollo 17 sample-station soil data. In this work, we exploit this relationship to assess geologic and soil compositional variations at PAN sites and to assess possible heterogeneity of lithologies in the regolith at these sites. We present results for the calibration sites and initial results for one of the most prominent occurrences of PAN, in a location in the eastern Inner Rook Ring (IRR) of the Orientale basin.

1.1 Significance

Relevant science questions include: (1) What is the role of "purest anorthosite" in the makeup of the lunar crust? (2) How is PAN related spatially to other crustal rock types? (3) What was its origin? These questions have significance for how the lunar magma ocean solidified and differentiated, specifically the efficiency of plagioclase separation, owing to its low density and buoyancy in Fe-rich residual melt, and to the composition of the Moon's crust and thus its bulk composition. Our approach is to explore PAN localities, a primary crustal rock type exposed in uplift structures (central peaks, basin rings), identified by spectroscopic studies [2,6,7] and to conduct compositional analysis using combined NAC photometry and DTM data to compensate for the effects of topography on reflectance.

1.2 Purest Anorthosite

NIR spectroscopy measurements from recent missions reveal pure or nearly pure anorthosite (PAN) in uplift structures directly from the occurrence of an ~1.25 micron absorption and an absence of mafic mineral (pyroxene and olivine) features. Ohtake et al. (2009) [2] first showed a global distribution of PAN using SELENE data. Cheek et al. (2013) [6] and Donaldson Hanna et al. [7] used Moon Mineralogy Mapper (M^3) data coupled with laboratory and Diviner data, respectively. These studies showed that PAN is widely distributed across the lunar surface, but mainly in uplift structures (central peaks, crater rims, and ring massifs) in large impact craters and basins of the Feldspathic Highlands Terrane.

2. Results

Example results are shown in Figure 1. Single scattering albedo derived using local incidence and emission angles correct fairly well for slope effects, especially on Sun-facing slopes (fore slopes); however, slopes facing away from the Sun (back slopes) are not entirely corrected. Massif materials, with <1 wt.% FeO, have *w* values approaching 0.53, whereas values in the Maunder Fm., interpreted to be Orientale impact melt, are ~0.3 and correspond to 4.5 +/- 2 wt.% FeO [8]. Higher *w* values are associated with small, fresh impact crater materials.

Modeled values of *w* on the broad, Sun-facing fore slope of the large massif shown in Fig. 1, which appears to be a good exposure of PAN, range from 0.38 at the base to 0.5 at the summit. This variation could reflect compositional mixing of PAN with materials of the Maunder Fm. or of less mature PAN material at the top with more mature, but still very feldspathic, material downslope. We are evaluating such hypotheses using M^3 spectra, which exhibit absorption band variations that include deep and clear to poorly defined 1.25 μm absorptions, to poorly defined 1.25 μm absorptions, indicative of crystalline anorthite, to featureless spectra, which may be associated with more mature feldspathic soils.

3. Discussion

Materials associated with massifs of the Inner Rook Ring exhibit some of the highest *w* values on the lunar surface [4]. We selected this location as one of the first to study in detail because the massifs likely contain a high proportion of PAN [6]. Nevertheless, we observe variability in small "patches" that are not associated with topography, with *w* ranging from 0.4 to 0.5. In the hilly inter-massif terrain shown in Fig. 1, *w* values are lower, in some areas reaching as low as 0.3, consistent with Maunder Fm. values [8]. Perhaps these are areas where impact melt mixed with uplifted anorthositic rocks.

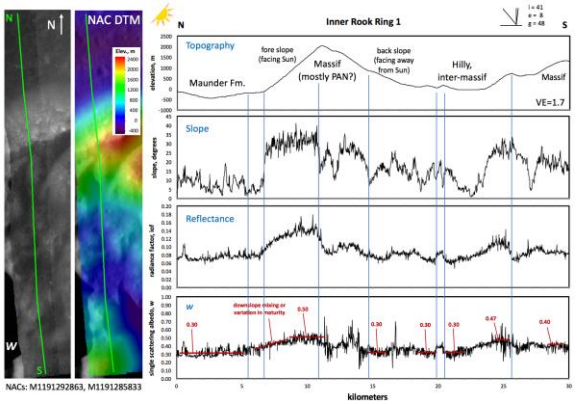

Figure 1: Example of data from analysis of NAC photometry at IRR1 site (Cen Lat: 19.516°S, Cen Lon: 86.607°W). Single scattering albedo (*w*) computed using *local* incidence and emission extracted from DTM.

Conclusions and Future Work

Ongoing work includes assessing whether local variations in *w* correlate with mineralogical variations using M^3 data. Variations do occur at local (NAC) scale, but careful assessment is required to distinguish compositional from topographic and maturity effects.

Acknowledgements

We thank NASA for continued support of the LRO mission and the LRO mission operations team at Goddard Space Flight Center and the LROC operations team at ASU. We especially appreciate the expert work of the specialists who produce NAC DTMs at ASU.

References

[1] Ohtake, M. et al.: The global distribution of pure anorthosite on the Moon. Nature, Vol. 461, 236-241, 2009.

[2] Henriksen, M.R., et al.: Extracting accurate and precise topography from LROC narrow angle camera stereo observations, Icarus, Vol. 283, 122-137, 2017.

[3] Hapke, B.: Theory of Reflectance and Emittance Spectroscopy, Second Ed., Cambridge Univ. Press, New York, 2012.

[4] Watkins, R.N., et al.: Nonmare volcanism on the Moon: Photometric evidence for the presence of evolved silicic materials. Icarus 285, 169-184, 2017.

[5] Hahn, T., et al.: Regional-scale LROC NAC photometric analysis of the Taurus-Littrow valley: A coordinated investigation and calibration using soil compositional data. Lunar and Planetary Science Conference 49, #2637, Houston, Texas, 2018.

[6] Cheek, L. et al.: The distribution and purity of anorthosite across the Orientale basin: New perspectives from Moon Mineralogy Mapper data. J. Geophys. Res. 118, 1805-1820, 2013.

[7] Donaldson Hanna, K. et al.: Global assessment of pure crystalline plagioclase across the Moon and implications for evolution of the primary crust J. Geophys. Res. 119, 1516-1545, 2014.

[8] Spudis, P. et al.: Geology and composition of the Orientale Basin impact melt sheet. J. Geophys. Res. 119, 19-29, 2014.